University of Tartu
Faculty of Science and Technology
Institute of Chemistry
Chair of Physical Chemistry

Annabel Raudsepp

Characterisation of Platinum Catalysts Based on Waste Tire Derived Carbons

Master's thesis (30 ECTS)

Material Science and Technology

Supervisors: Rutha Jäger, PhD
Jaak Nerut, PhD

Tartu 2024

Abstract

Rehvipurust sünteesitud süsinikul põhinevate plaatina katalüsaatorite karakteriseerimine

Töös uuriti hapniku redutseerumise reaktsiooni (ORR) aktiivsust vanarehvidest sünteesitud süsnikalusmaterjalile sadestatud plaatinakatalüsaatoritel. Kuna vanarehvidest saadud süsinik sisaldas erinevaid lisandeid, siis prooviti neid leelise- ja happetöötlusega eemaldada. Plaatina sadestamiseks kasutati kahte süsinikku ja kahte sünteesimeetodit. Saadud süsinikele ja katalüsaatormaterjalidele teostati füüsikaline ja elektrokeemiline karakteriseerimine. Pöörleva ketaselektroodi meetodiga uuriti materjalide ORR-i kineetikat 0,1 M $HClO_4$ lahuses. Sünteesitud Pt katalüsaatorite aktiivsust testiti prootonvahetus-membraaniga kütuseelemendi (PEMFC) ühikrakus. Suurim maksimaalne võimsustihedus (0,42 W cm^{-2}) ja voolutihedus (0,35 A cm^{-2} 0,7 V juures) saavutati materjaliga, milles Pt nanoosakesed olid sadestatud süsinikalusmaterjalile, mis sisaldas rohkem algsest rehvipurust tulenevaid jääke.

Märksõnad: ORR, rehvipurust sünteesitud süsinik, plaatina, komposiitkatalüsaator, PEMFC

CERCS: T140 Energeetika, T152 Komposiitmaterjalid, P401 Elektrokeemia

Characterisation of Platinum Catalysts Based on Waste Tire Derived Carbons

The aim of this work is to investigate the activity of oxygen reduction reaction (ORR) on platinum catalysts deposited on carbon support material synthesised from waste tires. Since the carbon obtained from waste tires contains some impurities, it was tried to remove these impurities with acid and alkaline treatment and to compare support carbons with and without additives. Two support carbons and two synthesis methods were used to deposit platinum. The obtained carbons and catalyst materials were subjected to physical and electrochemical characterization. The ORR kinetics of the materials in 0.1 M $HClO_4$ solution was investigated by the rotating disc electrode method. The activity of the synthesized Pt catalysts was tested in a proton-exchange membrane fuel cell (PEMFC) single cell. The highest maximum power density (0.42 W cm^{-2}) and current density (0.35 A cm^{-2} at 0.7 V) were obtained with the material in which Pt nanoparticles were deposited on carbon containing more residues from the granulated material of waste tires.

Keywords: ORR, waste tire derived carbon, platinum, composite catalyst, PEMFC

CERCS: T140 Energy research, T152 Composite materials, P401 Electrochemistry

Contents

Abbreviations

Ads/des – adsorption/ desorption

BET – Brunauer-Emmett-Teller

CV – cyclic voltammetry

ECA – electrochemically active surface area

EIS – electrochemical impedance spectroscopy

EDL – electrical double layer

FWHM – full width at half maximum

GDL – gas diffusion layer

$H_2PtCl_6 \times 6H_2O$ – hexachloroplatinic acid (or Pt complex)

HR-SEM – high-resolution scanning electron microscopy analysis

IPA – isopropyl alcohol

MEA – membrane electrode assembly

OCV – open circuit voltage

ORR – oxygen reduction reaction

PEMFC – proton-exchange membrane fuel cell

RDE – rotating disc electrode

RHE – reversible hydrogen electrode

SEM – scanning electron microscopy

SEM-EDX - scanning electron microscopy with energy dispersive X-ray analysis

TGA – thermogravimetric analysis

XRD – X-ray diffraction analysis

2D-NLDFT-HS – Two-Dimensional Non-local Density Functional Theory for Heterogeneous Surface

Introduction

We live in a world where the energy sector is responsible for about three-quarters of today's greenhouse gas emissions and is pivotal in addressing humanity's paramount challenge: climate change. A lot of pollutants such as carbon dioxide and other harmful emissions are released into the air because of fossil fuel use, therefore we need to change the way how we produce, transport, and consume energy [1,2]. One possible solution to the problem would be to increase the share of renewable energy. Hydrogen's high energy density, ample availability on Earth, and emission-free water as a byproduct of combustion make it a prime candidate for powering transportation systems as a synthetic energy carrier [3]. Proton-exchange membrane fuel cell (PEMFC) is used in electrical vehicles. During the working of this energy conversion device, chemical energy is converted into electrical energy by using hydrogen as fuel and oxygen from the air as oxidiser. PEMFC catalyst layers contain precious metals like Pt, which are supported on a porous carbon [4]. However, since Pt is such a rare element on earth, development work is underway to reduce its quantity and replace it with new active catalysts.

Another problem the world faces is waste management and recycling. As the demand for transportation is increasing, more and more old tires are generated yearly [5]. Although landfilling is the least preferable choice for environmental preservation due to its associated public health hazards, and its pollution of water, air, and soil, as well as its contribution to global warming, it remains the predominant method of waste management. And so, most waste tires are also landfilled, but we should seek opportunities to create something new and valuable out of them [6].

This master's thesis aimed to investigate platinum catalysts based on waste tire derived carbons and identify the best oxygen reduction reaction (ORR) catalyst in a three- and two-electrode system using different carbon supports and two Pt deposition methods. The carbon from waste tires contains different impurities. Therefore, the second goal of the thesis was to carry out additional treatments of the carbon support material to remove impurities. It was hypothesised that those impurities in carbon support may adversely affect the oxygen reduction activity of the synthesised Pt catalyst. Therefore, carbon materials were also investigated. The synthesised catalysts and carbons were physically characterised using scanning electron microscopy (SEM), X-ray diffraction analysis (XRD), thermogravimetric analysis (TGA), and N_2 sorption analysis methods.

1. Literature Overview

1.1. Proton-Exchange Membrane Fuel Cell

A PEMFC is a device that uses air or oxygen for its work and hydrogen as fuel and uses them to convert chemical energy into electrical energy. Apart from electricity, the products are also heat and water, so there are no harmful emissions to the environment. PEMFC is a low-temperature fuel cell, it works in the temperature range of 60-80 °C. The PEMFC employs a polymer membrane as an electrolyte. While this membrane doesn't conduct electricity, it's highly efficient at conducting hydrogen ions. The membrane (Nafion) is made from a fluorocarbon polymer chain akin to Teflon, with attached sulfonic acid groups. These acidic groups are covalently bonded to the polymer. However, the protons within these acidic groups can freely move across the membrane. This membrane, together with the catalyst layer on both sides (anode and cathode), forms the most crucial part of the PEMFC, known as membrane electrode assembly (MEA). [7,8] MEA can also be 5-layered, which means that in addition to the catalyst layers and the membrane, there are also gas diffusion layers (GDLs) on both sides, which ensure an even distribution of gases. MEA catalyst layer preparation involves two major techniques. One is the direct application of the catalyst suspension onto the electrolyte membrane, and the other is coating the GDL. [9] The thickness of GDL is mostly in the range of 150-400 μm. Its thickness and structure affect the electrical and thermal conductivity of the GDL and the mass transport within the GDL. GDLs can be made of carbon cloth or carbon paper coated with a hydrophobic microporous layer containing carbon and Teflon. This microporous layer ensures effective transport of the resulting water from the electrode into the diffusion medium and avoids water condensation. [8]

PEMFC's working principle is as follows (Figure 1). Hydrogen is fed to the anode, where hydrogen is oxidised into protons and electrons are released.

Anode: $$2\ H_2 \rightarrow 4\ H^+ + 4\ e^- \quad (1)$$

Protons are transported to the cathode through the electrolyte membrane and electrons move to the cathode along the circuit. At the cathode, the oxygen (from the air) is reduced to water, while heat is released. [7]

Cathode: $$O_2 + 4\ H^+ + 4\ e^- \rightarrow 2\ H_2O. \quad (2)$$

For both ORR at the cathode and the hydrogen oxidation reaction at the anode, catalyst materials containing platinum, which is the most effective catalyst, are used. Since the reaction of the cathode is considerably slower than that of the anode, a catalyst with a higher loading is also needed. [10,11]

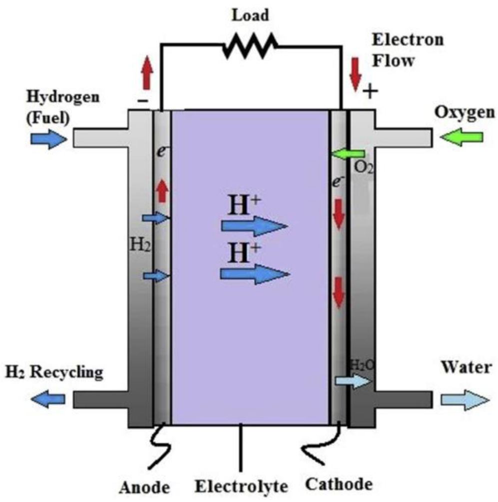

Figure 1. Scheme of the working principle of a proton-exchange membrane fuel cell [12].

1.2. PEMFC Catalysts and Catalyst Supports

Currently, due to their superior activity compared to all other metals, the most widely used catalysts in PEMFCs are platinum and its alloy-based catalyst materials (usually supported on carbon particles) [13–15]. The biggest disadvantages of Pt are its very high cost and its scarcity on Earth. These factors drive efforts to minimise its use and to seek alternative solutions. Despite extensive research into platinum-free electrocatalysts, including non-noble transition metals, metal nitrides, and nanocarbon-based metal-free electrocatalysts, their insufficient performance and stability render them unfit for commercial use in transportation fuel cells for the time being [16]. Pt, on the other hand, is very durable during hydrogen oxidation at the anode and ORR at the cathode.

The performance of the catalyst is also related to its surface area. Platinum nanoparticles provide a high surface area, which improves the performance of the fuel cell. [13,17] One of the most widely used carbon support materials for PEMFC catalysts are carbon blacks (e.g. Vulcan XC-72 and EC300 Ketjenblack) because of their low cost, great performance and high conductivity. However, carbon blacks may require additional processing, for example additional activation to increase their catalytic activity, for example doping with nitrogen or Mn which results in more graphitic and corrosion-resistant carbon. [15,18,19]

The design and performance of Pt catalysts utilised in PEMFCs are significantly influenced by the structure and form of the carbon. The unique porous structure of mesoporous carbons enhances oxygen transportation, while graphitisation ensures higher stability. The combined effect of Pt alloys and heteroatom doping of mesoporous carbons not only offers an excellent anchoring surface for platinum nanoparticles but also enhances their activity. Additionally, incorporating Pt alloys into mesoporous carbon reduces the agglomeration of nanoparticles, maximizes the surface area of nanoparticles, and establishes an efficient charge transfer pathway, thereby minimising mass transport resistance. Nonetheless, the restricted durability of carbon supports presents a substantial obstacle in achieving the extended lifespan required for PEMFC catalysts. Carbon materials also have a disadvantage: carbon supports are prone to corrosion in fuel cells, resulting in detachment, agglomeration, and dissolution of Pt nanoparticles, leading to electrochemical surface area loss and decreased catalytic activity. [15,18,19]

One possible carbon-based support materials are carbon nanotubes, which have a much higher electronic conductivity than carbon black because, in the structure of nanotubes, carbon is in a nearly 100% sp^2 hybridised state. The multi-walled carbon nanotubes, which have a lower surface area but higher electronic conductivity, are most commonly used in PEMFCs. Furthermore, carbon nanotubes have less impurities than carbon blacks. The disadvantage of carbon nanotubes is that sp^2 hybridisation complicates Pt nanoparticle deposition due to the limited availability of functional groups and surface defects for anchoring Pt nanoparticles. Among mesoporous carbons, ordered mesoporous carbons, colloid-imprinted carbons, carbon nanofibres and carbon nanocoils are also used as support materials. [20]

Waste tire derived carbons can be considered as a cost-effective and environmentally sustainable choice for carbon support material [21–23]. Every year, one billion old tires are thrown away. However, with a continuously expanding population and a increasing demand for vehicles, the accumulation of used tires continues to rise [24]. Therefore, the old tires are a source of carbon material that will not run out anytime soon. Currently, most used tires are stored in landfills, and a significant portion is burned for energy [25]. The burning of tires emits very harmful emissions into the environment, and thus more effective solutions for tire recycling should be found. In addition, it is possible to shred tires and use the resulting material to make rubber mats. However, to effectively recycle tires, it is necessary to expand the range of products obtained from used tires. The recycling of old tires is complicated by their composition, which typically consists of rubber (approx. 47 wt%), carbon black (approx. 21.5 wt%), steel (16.5 wt%), textiles such as polyester and nylon fibres (5,5 wt%) and organic and inorganic additives such as plasticisers, anti-ageing agents, sulphur and zinc oxide (approx. 9.5 wt%) [6]. Intensive efforts are underway to find recycling solutions for the textile fibre and rubber components. For example, the recycling of textiles as additives to sound absorbing materials, bituminous conglomerates, concrete production, plastic materials, and soil reinforcement has been studied [5]. One option is pyrolysis of old tires, which provides higher energy efficiency [5]. In addition, this method produces fewer gaseous pollutants compared to burning tires, thus reducing the demand for combustion gas removal. Pyrolysis of tires involves their thermal decomposition under non-oxidative conditions (inert atmosphere or vacuum). The chemical products created during this process, such as tire derived carbon, can serve as starting materials for other applications. Besides the possibility of using the carbon obtained from old tires as a support material for PEMFC catalysts, the use of this carbon as the anode material in lithium batteries has also been investigated [26]. Furthermore, the use of waste tire derived carbon as a supercapacitor electrode material has been investigated [22].

In this study, carbon materials were synthesised from waste tire granules (from which fibre and steel residues have been previously removed), and the obtained carbons were used as a support material for the synthesis of Pt catalysts for PEMFC applications.

1.3. Physical Characterisation Methods

1.3.1. Scanning Electron Microscopy

SEM is a highly adaptable and extensively utilised method among surface analysis techniques. It offers the unique ability to examine both the structure and composition of a wide range of materials. SEM measurements are done in a vacuum environment to increase the mean free path of electrons. SEM apparatus consists of the electron gun, anode, lenses, scanning coils, three detectors and a sample chamber (Figure 2). The most used electron gun is the tungsten filament. This filament is heated up to approximately to 2500 °C, causing it to emit electrons. These electrons are then accelerated down the column with the help of an anode. Magnetic lenses focus electrons into a narrow electron beam. These lenses also control the amount of electrons that reach the sample. The purpose of the scanning coil is to move the electron beam so that the sample is scanned row by row. The objective lens determines the focusing of the electron beam. Each point of the sample surface that is bombarded with electrons is emitting different signals, including secondary electrons, backscattered electrons, and characteristic X-rays, which are then detected. By using these signals, we can create an image of the surface. Secondary electrons are created when the primary electron beam interacts with the surface of the sample, causing electrons to be ejected from the surface. Secondary electrons, having low energy, originate from the near-surface region (0-5 nm depth). Secondary electrons are collected by the secondary electron collector, providing information about sample's topography. Backscattered electrons are generated when the primary electron beam interacts with the sample in a manner where they retain much of their energy. These electrons emerge in a direction similar to that of the primary electron beam, and backscattered electrons originate deeper from the sample, typically at depths of 0-400 nm. Backscattered electrons are collected with the backscattered electron detector, providing information about differences in atomic number. When primary electron beam energy is sufficient then it will excite the atom of the sample and during the relaxation process characteristic X-rays are generated (at depths of 0-2 µm). These X-rays are collected with energy-dispersive X-ray detector and this signal provides information about the chemical composition of the sample (elements, their distribution and concentration). [27,28]

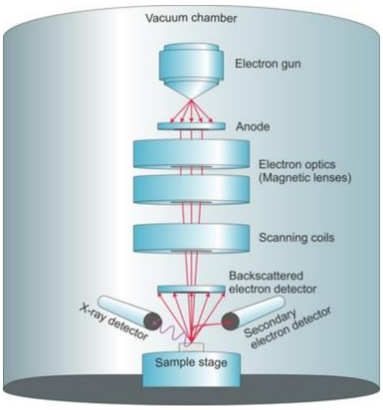

Figure 2. Scheme of a scanning electron microscope [29].

1.3.2. X- Ray Diffraction Analysis

XRD is a physical characterisation method of materials that allows the study of the phase composition, size of crystallites, the orientation of crystallites, crystal lattice structure and lattice parameters, close arrangement of atoms, internal stresses, and coefficient of thermal expansion. XRD can be used for quantitative and qualitative analysis. X-ray diffractometers consist of an X-ray tube, a sample holder, and a detector. During the analysis, the sample is irradiated with a monochromatic X-ray beam, and the resulting diffracted beam is recorded. Figure 3 explains the principle of X-ray diffraction. Monochromatic X-ray radiation is reflected within the crystal only in specific directions, where the condition of constructive interference is met. A parallel beam of X-rays strikes the atomic planes at an angle θ and is reflected from them at the same angle. The first beam is scattered from the O atom, and the second beam is scattered from the G atom. The reflected rays must fulfil the condition of constructive interference, meaning their phases must coincide. To achieve this, the difference in their optical path lengths must be an integer multiple of the wavelength. OF and OH are drawn perpendicular to the incident rays, creating an optical path length difference FG + GH between the rays reflecting from two neighbouring planes. Here, FG = GH = $dsin\theta$ from which Bragg's formula follows:

$$n\lambda = 2d\sin\theta, \tag{3}$$

where n is an integer, λ is the wavelength of the incident X-ray beam, d is the distance between the atomic planes, and θ is the angle between the atomic plane and the incident radiation. [30–32]

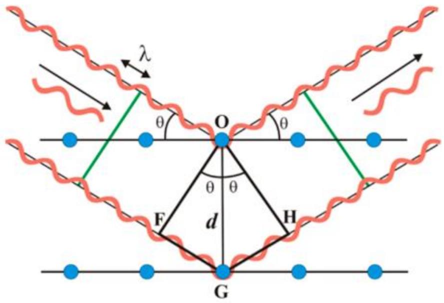

Figure 3. Schematic diagram explaining Bragg's law [33].

XRD can be used to determine the crystallite size, D, from the diffraction line width using the Scherrer's formula:

$$D = \frac{K \times \lambda}{\beta \times \cos\theta}, \tag{4}$$

where K is the Scherrer constant and β is the full width at half maximum (FWHM). The diffraction line broadens as the crystallite size decreases due to the insufficient number of atomic planes in the crystallite. This leads to a scenario where complete destructive interference doesn’t occur, even with a minor deviation from the Bragg angle. Consequently, the FWHM of the reflection increases, observed on the diffractogram as a wider reflection with a reduced intensity. In contrast, for larger crystallites, rays diffract on both sides of the Bragg angle, resulting in non-constructive interference due to the summation of many diffracted rays from atomic planes. [34]

1.3.3. Thermogravimetric Analysis

TGA measures the variation in mass (either an increase or decrease) and the speed of this variation, based on factors such as duration, temperature and a gas environment (such as air, N_2, CO_2, Ar, etc.). TGA is used to study the thermal and oxidative stability of materials, the composition of multi-component systems, residual mass, decomposition kinetics of materials, volatiles, and moisture content of materials. The most commonly used type of TGA is dynamic thermogravimetry, where a sample is heated in an environment with the temperature adjusted in a pre-set way, typically at a linear rate. The second type is static or isothermal thermogravimetry, where the weight of the sample is recorded over time while maintaining a constant temperature. The third type is quasistatic thermogravimetry, where the sample is heated to constant weight at each series of increasing temperatures. The TGA apparatus consists of a highly sensitive scale to measure changes in the weight, sample holder or crucible (made from Pt, Al, Al_2O_3, graphite, stainless steel etc.), thermocouple to control the temperature and a programmable furnace to control the temperature of the sample environment. TGA results are typically displayed by a plot of mass change in mass percent (*y*-axis) versus time or temperature (*x*-axis) and are commonly referred as TGA curves. Several factors can influence the shape of these curves, including instrumental factors such as furnace atmosphere and heating rate, as well as sample characteristics such as sample particle size and weight, sample holder, heat of reaction, and compactness of the sample. [35–37]

1.3.4. Nitrogen Sorption Analysis

Gas sorption analysis is a well-known method for determining the specific surface area of solid porous/non-porous powders. The latter is typically determined by calcualting the quantity of an adsorbed inert gas that forms an imaginary single-molecule layer at the interface between the solid and vapour. The adsorption is a dynamic equilibrium process. An ideal adsorbate would exhibit uniform adsorption strength across all types of surfaces present in the sample. The most commonly used adsorbate is nitrogen (at liquid nitrogen temperature) due to its easy availability and chemical inertness. However, a disadvantage of using nitrogen is its low temperature of the normal boiling point, which results in slow mass transport processes, causing nitrogen molecules to take a longer time to penetrate small pores. Other adsorbates such as argon, xenon, and krypton are also used. [38–41]

The adsorption isotherm should be fitted using a suitable physical model that accounts for both the adsorbent (solid) and the adsorbate (gas). The most commonly used adsorption model is the Brunauer-Emmet-Teller (BET) equation. The BET theory allows for the prediction of multilayer adsorption, heat of adsorption and specific monolayer adsorption capacity on different adsorption layers. However, the main issue with this model arises from its three underlying assumptions: first, that adsorption has reached equilibrium; second, that the surface is homogeneous; and third, that the surface of the adsorbent is flat. The specific surface area, S_{BET}, of the material can be determined using the BET method.

BET equation in the linear form is expressed as [40]:

$$\frac{p}{n^{\mathrm{a}} \times (p^0 - p)} = \frac{1}{n_{\mathrm{m}}^{\mathrm{a}} \times C} + \frac{(C-1)}{n_{\mathrm{m}}^{\mathrm{a}} \times C}\frac{p}{p^0}, \tag{5}$$

where n^{a} is the amount of adsorbed substance at the relative partial pressure $\frac{p}{p^0}$, $n_{\mathrm{m}}^{\mathrm{a}}$ is the monolayer capacity, and C is the BET constant. Using the capacitance of a single layer, the S_{BET} value can be calculated [40]:

$$S_{\mathrm{BET}} = \frac{n_{\mathrm{m}}^{\mathrm{a}} \times N_{\mathrm{A}} \times a_{\mathrm{m}}}{m}, \tag{6}$$

where N_a is is Avogadro's number, a_m is the molecular cross-sectional area, and m is the mass of the adsorbent.

The other important parameters are the micropore volume, V_{micro}, which represents the pores with a diameter smaller than 2 nm, and the total pore volume, V_{tot}. V_{tot} is typically determined at the point where the relative pressure of nitrogen is 0.95. [38–41] Additionally, the specific surface area, S_{DFT}, and total pore volume, V_{DFT}, can be determined using the Two-Dimensional Non-local Density Functional theory for Heterogeneous Surface (2D-NLDFT-HS) model which takes into account that the adsorbing surface is energetically and structurally heterogeneous. [38]

1.4. Electrochemical Research Methods

1.4.1. Cyclic Voltammetry and Electrochemically Active Surface Area of Platinum Nanoparticles

Cyclic voltammetry (CV), widely employed in electrochemistry for investigating redox reactions and capacitive processes, utilises a three-electrode system comprising a working electrode (which can function as both an anode and a cathode), an auxiliary electrode (such as a platinum mesh), and a reference electrode (like a reversible hydrogen electrode (RHE)). The cyclic voltammogram is a dependence of current density (mA cm^{-2}) on electrode potential at specific electrode potential scan rates (mV s^{-1}) [42–44]. The voltammogram of the redox pair has current density peaks that describe the electrochemical reactions taking place at the electrode surface. Initially, the voltammogram shows an increase in current density $|j|$ resulting from the reaction being accelerated by applying a higher over-potential. Due to the change in potential, there comes a point where the reactant diffusion rate to the electrode decreases as it reacts there. Near the electrode, the diffusion layer becomes depleted of reagent, resulting in a decrease of the concentration gradient. Therefore, we observe a decrease in the current density $|j|$ on the voltammogram [42]. The height and width of the peaks depend on the reversibility of the reaction, the concentration and diffusion coefficient of the reagent, electrolyte, the material of the electrode and the electrode potential scan rate [45,46].

The cyclic voltammogram of the Pt catalyst is used to calculate the electrochemically active surface area (ECA) of platinum nanoparticles. There is an area of hydrogen adsorption and desorption (ads/des) at the electrode potentials less positive than 0.45 V vs RHE and an oxygen ads/des area at electrode potentials more positive than 0.60 V vs RHE [45,47–49]. The area between these two regions is the so-called electric double layer area (EDL).

The formula used to calculate ECA is:

$$ECA = \frac{q_{\mathrm{Pt-H}}}{q_{\mathrm{Pt-H,poly}} m_{Pt}}, \tag{7}$$

where $q_{\mathrm{Pt\text{-}H,poly}}$ is the charge required to form an adsorbed monomolecular layer of hydrogen on an ideally smooth Pt surface (210 μC cm^{-2}) [49], m_{Pt} is the mass of Pt on the electrode surface, $q_{\mathrm{Pt\text{-}H}}$ is the hydrogen ads/des charge and can be found from the formula:

$$q_{\mathrm{Pt-H}} = \int_{E_2}^{E_2} C_{\mathrm{EDL}} \mathrm{d}E - C_{\mathrm{EDL}}(E_2 - E_1), \tag{8}$$

where E_1 is the potential in the middle of the Pt EDL region, E_2 is the potential at the end of the hydrogen ads/des area and C_{EDL} is the average EDL capacitance, which is assumed to be constant and independent of the electrode potential. To find the capacitance, C, the current density, j, is divided by the electrode scan rate, v. [45,47–49]

1.4.2. Rotating Disc Electrode Method

The mechanisms and kinetics of electrochemical reactions can be investigated using the rotating disc electrode (RDE) method. The main component of RDE is a cylindrical working electrode made of for example glassy carbon, which is surrounded by an inert insulating material, typically Teflon. The electrode is submerged in the electrolyte solution and set into motion through rotation facilitated by a rotator. This rotation causes the electrolyte solution move towards the electrode due to the rotation of the electrode. To study the catalysts, the electrode is coated with the material under investigation. [50]

If the flow of the electrolyte solution is laminar and the reaction rate is determined by mass transport, then the diffusion current density, j_{D}, can be found from Levich's formula. In the case of ORR, it is expressed as follows [45,51,52]:

$$j_{\mathrm{D}} = -0.62\, n\, \mathrm{F}\, D^{2/3} \omega^{1/2}\, \upsilon^{-1/6}\, c = -B\, \omega^{1/2}, \tag{9}$$

where n is the number of electrons transferred per O_2 molecule, F is the Faraday number (96485 C mol^{-1}), D is the diffusion coefficient of O_2 (1.9×10^{-5} cm^2 s^{-1} in 0.1 M $HClO_4$), ω is the angular velocity of the electrode rotation, υ is the kinematic viscosity of the solution (0.01 cm^2 s^{-1} in 0.1 M $HClO_4$ solution at 22 °C [53–55]), c is the concentration of O_2 in the solution (1.26 mol m^{-3} in 0.1 M $HClO_4$ solution at 22 °C [53–55]) and $B = 0.62n\mathrm{F}D^{2/3}\upsilon^{-1/6}c$ is known as Levich's constant.

If reaction kinetics are controlled by both slow charge transfer and mass transfer steps then the total current density, j, can be described by the Koutecký -Levich equation [53–55]:

$$\frac{1}{j} = \frac{1}{j_\mathrm{k}} + \frac{1}{j_\mathrm{D}} = \frac{1}{j_\mathrm{k}} + \frac{1}{-B\,\omega^{1/2}}, \qquad (10)$$

where j_k is the kinetic current density.

2. Experimental

2.1. Synthesis

2.1.1. Carbon Synthesised from Waste Tires

To prepare Pt/C catalysts, two different carbon materials were used as supports. Instructions found in the literature were used for carbon synthesis [56,57]. First, carbon material was synthesised from waste tire granules (Imdex A/S, Denmark) with a size of 0.8-3.0 mm, from which the textile and steel components had previously been removed. Waste tire granules were placed on a quartz crucible in a tube furnace (Carbolite). The furnace temperature was increased at a rate of 2 °C min^{-1} up to 1000 °C. Pyrolysis occurred at 1000 °C in an argon environment (99,999%, As Linde Gas, flow rate 145 cm^3 min^{-1}) for 3 h, yielding 37% carbon. The resulting carbon was ground in a ball mill (Fritsch, Pulverisette 6) at a rotation speed of 400 rpm for 30 min using YSZ balls (5 pcs., 20 mm). [58,59] The resulting carbon material is referred to as **C1** in the thesis. Joel Indrek Martin Laanemäe synthesised the carbon **C1**.

Due to the presence of multiple residues in the **C1** material (chapter 3.1.), enhancements were made to the carbon synthesis method (Figure 4). First the waste tire granules were washed in distilled water in an ultrasonic bath (Elma Schmidbauer GmbH Elmasonic P 30 H/ Pmax 320 W, 37 kHz, temperature 21 °C) in a beaker. Subsequently, the beaker containing distilled water and granules was placed on the stove and heated until the granules floated to the surface, causing the water to turn yellow. Next, the tire granules were rinsed with Milli-Q^+ water (18.2 MΩ cm). Then, the previous steps were repeated twice more, followed by drying (BINDER FD 53 E2, 60 °C for 2 h and 100 °C for 15 h and at room temperature for 24 h). The product was pyrolysed in a tube furnace (450 °C 3h, flow rate 200 cm^3 min^{-1}) in an argon environment. The resulting carbon material is named **C2** in the thesis.

The carbon material that underwent the first pyrolysis (**C2)** was treated with an alkaline solution for 1 h, using 150 cm^3 1 M KOH (prepared from solid KOH, purity 89.7%, Lachner). This step was incorporated into the carbon synthesis process to activate the material and eliminate impurities (SiO_2) from the waste tire granules. [60] For that, **C2** was placed in a Teflon container, which was filled with KOH solution and placed on a stove (heated up to 60 °C). After 1 h, the stove was turned off and the mixture was left to stir with a magnetic stirrer for about 24 h. By this time, the carbon had formed a uniform suspension. The suspension was vacuum filtered with 1200 cm^3 Milli-Q^+ water (to get rid of KOH) and then dried in a vacuum drying cabinet (110 °C and 50 bar). The resulting carbon material is named as **C3**.

Since the synthesised carbon **C1** had a low specific surface area, it was decided to use pore formers in carbon synthesis. [57,58]. Therefore, the resulting carbon **C3** was ball milled with $ZnCl_2$ (Sigma-Aldrich, ≥97%), hydroxyapatite (Sigma-Aldrich, ≥96%) and isopropyl alcohol (IPA) (LashNer, 99.99%) using 250 pcs YSZ 5 mm balls (2×15 min grinding cycles, 350 rpm,). IPA was then added to the suspension obtained from the ball mill, mixed with HIGH-SHEAR mixer (IKA S25N-10G, 60 min), and in an ultrasonic bath (30 min), and dried (80 °C overnight). Next synthesis step involved pyrolysis at 700 °C for 1 h with an argon flow rate 200 $cm^3\ min^{-1}$. To eliminate impurities from material, acid washing was conducted [57]. The acid treatment, lasting 24 h, was conducted using 900 cm^3 of 1 M HNO_3 (prepared from 67-70% HNO_3, Fisher Chemical) solution by heating the reaction mixture in an oil bath with an vertical condenser and stirring with a magnetic stirrer. The suspension was vacuum filtered and washed with Milli-Q^+ water and dried in a vacuum (100 °C, 50 mbar). The resulting carbon material is named as **C4**.

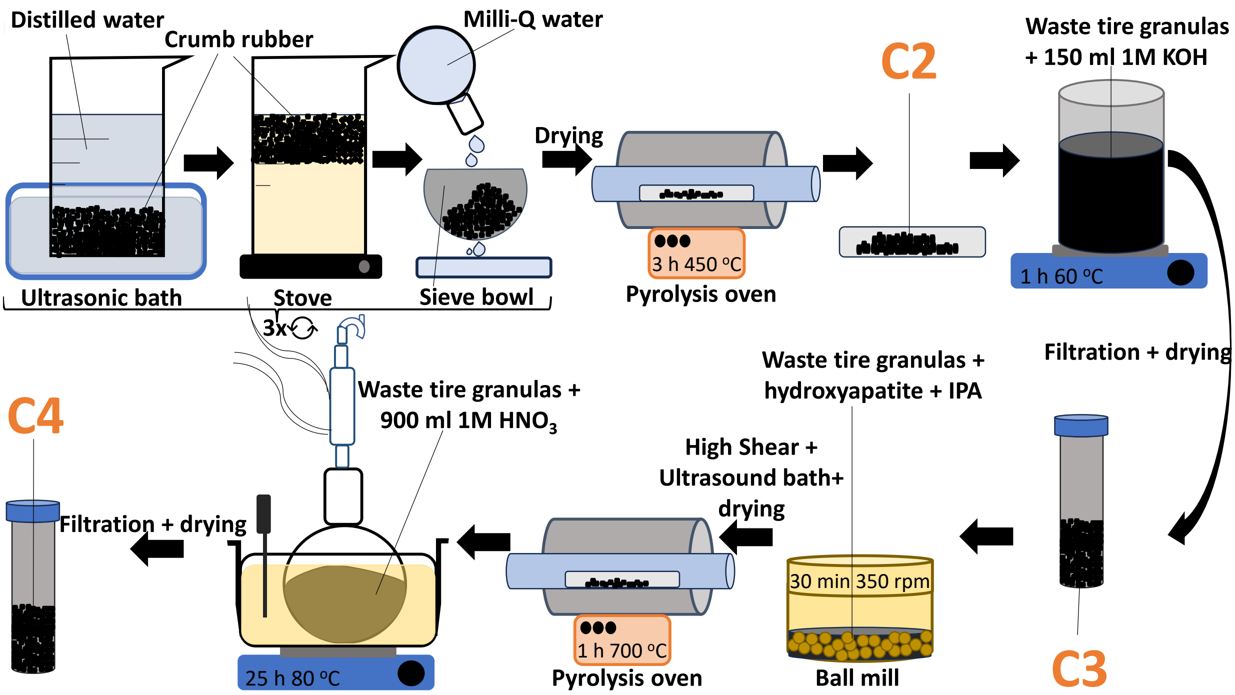

Figure 4. Schematic illustrating the improved carbon synthesis method.

2.1.2. First Synthesis of Catalyst Materials

60 wt% Pt catalyst materials were synthesised by two different methods. The main differences between these synthesis methods are as follows. The first synthesis involved the deposition of Pt nanoparticles on carbon from a reaction mixture i.e. the synthesised Pt nanoparticles and carbon were in the same reaction mixture from the beginning. The temperature of the solution was raised smoothly up to the synthesis temperature of 110 °C. In the second synthesis,

Pt nanoparticles were synthesised separately and then deposited on carbon. The reaction mixture was placed in an already preheated oil bath at a temperature of 160 °C.

In the first synthesis (Figure 5) [61–63], an aqueous solution of NaOH (0.618 g; 99,99% metal basis, Na_2CO_3 < 1%, Sigma-Aldrich)) was prepared in a mass ratio of 1 : 1 and 100.5 cm^3 of ethylene glycol (≥99,5%, Sigma-Aldrich) was added. 0.200 g of either carbon material **C1** or **C4** was then added to the resulting mixture, followed by mixing in an ultrasonic bath for 15 min. After that, the synthesis mixture was stirred and saturated with argon. Meanwhile, 0.800 g of the platinum complex ($H_2PtCl_6 \times 6\,H_2O$, *crystalline*, 99.9%, Alfa Aesar) was dissolved in 5 cm^3 Milli-Q$^+$ water and the resulting solution was added dropwise (using a syringe pump) to the reaction mixture over about 20 min. The mixture, which was in a round bottom flask equipped with a vertical condenser, was stirred by heating in an oil bath at 110 °C under an argon atmosphere for 2 h. Afterwards, the reaction mixture was cooled, and then a solution comprising 30 cm^3 of Milli-Q$^+$ water and 1.02 cm^3 of concentrated HCl (≥ 37%, Sigma-Aldrich) was added. The reaction mixture was stirred for another 20 min before vacuum filtration. Demineralised water (700 cm^3) was added to speed up the filtration. After the filtration, the product was dried in a vacuum drying cabinet (100 °C, 50 mbar) for 24 h. The dry catalyst material was weighed, and the yield percentage was 95%. Depending on the carbon support used (**C1** or **C4**), the catalyst material **S1** or **S2** was obtained, respectively.

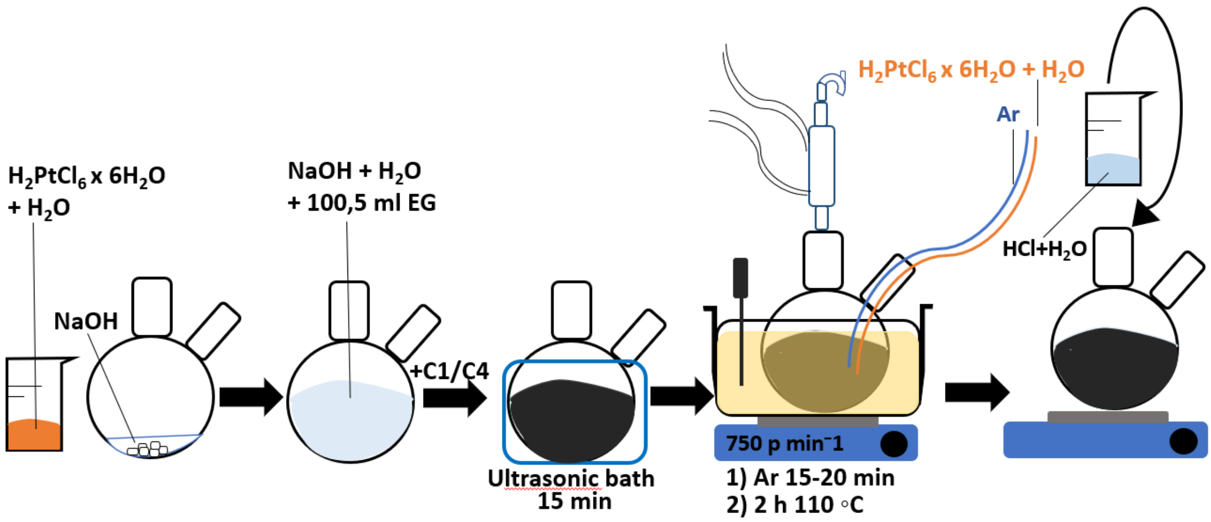

Figure 5. Schematic illustrating the first catalysts synthesis method.

2.1.3. Second Synthesis of a Catalyst Material

A scheme illustrating the second synthesis method [64] is provided in Figure 6. In one flask, 0.414 g of the platinum complex was dissolved in the 40.0 cm^3 of ethylene glycol and in another flask, 0.320 g of NaOH was dissolved in the same volume of ethylene glycol. The solutions of the Pt complex and NaOH solution were then combined in a round reaction flask and stirred in a preheated oil bath for 90 min at 160 °C. After heating, the mixture was allowed to cool down. The suspension was divided between the required amount of centrifuge tubes (45 ml), and 1 M HCl (prepared from ≥ 37% HCl) was added to fill up the tubes. The mixture was centrifuged for 5 min at 5000 rpm (Domel Centric 250) and the solution over the Pt nanoparticles was discarded. The washing of Pt nanoparticles with 1 M HCl was repeated three times, to yield purified Pt nanoparticles. Next, 0.191 g of carbon **C4** and acetone (purity min. 99.5%, OKKO Products) were mixed in a rotatory evaporator flask and sonicated (37 kHz, temperature 21 °C). The nanoparticles were then added to the flask using small amount of acetone. The mixture of nanoparticles and material **C4** was manually stirred in the flask and then dried in the rotary evaporator (Büchi R-100). Subsequently, the flask was placed in a vacuum-drying cabinet overnight. The material was mixed with water next day and the suspension was vacuum filtered and then dried again in a vacuum drying oven (for 5 h). Finally, the product was weighed (0.249 g, 99%), and the catalyst material was then crushed into a fine powder in a glass vial with a metal spatula. The resulting catalyst material is named **S3** in the thesis.

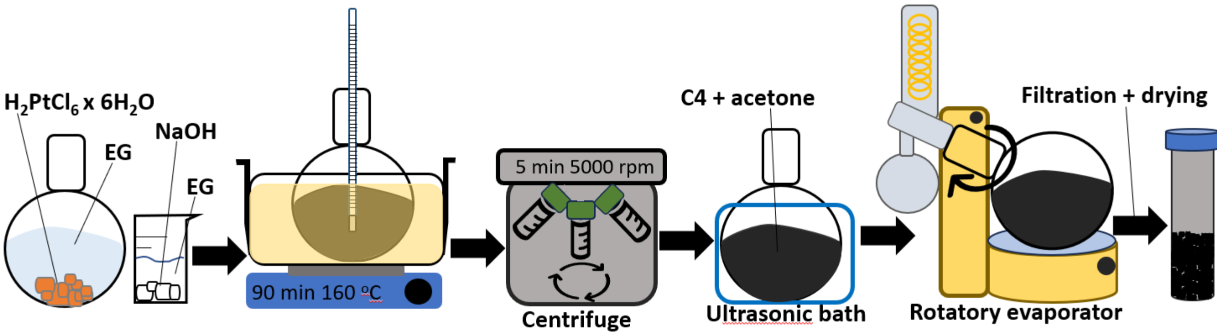

Figure 6. Schematic illustrating the second method of catalyst material synthesis.

All three synthesised materials were compared with the commercial material 60% Pt HSA Ketjenblack (FuelCellStore), which will be denoted by the letter **K** in the thesis.

2.2. Physical Characterisation of the Synthesised Materials

A high-resolution scanning electron microscope (Zeiss Merlin) equipped with an energy dispersive X-ray (EDX) microanalyser (Bruker EDX-Xflash®) was used for high-resolution scanning electron microscopy analysis (HR-SEM). For analysis, suspensions of carbon powders were prepared, and these samples were transferred to carbon tape. To prevent charging of the surface of the samples, to provide a homogeneous surface for analysis and imaging, and to promote the emission of secondary electrons for even conduction, the samples were coated with a 0.5 nm Au/Pd layer before the measurement [27,29]. Operating voltages of 8 keV and 3 keV were used for HR-SEM and SEM-EDX, respectively. HR-SEM and SEM-EDX measurements were carried out by PhD Olga Volobujeva at TalTech.

XRD measurements were performed with a Bruker D8 Advance diffractometer using nickel-filtered CuKα radiation (0.6 mm wide parallel beam, two 2.5° Soller slits, LynxEye strip detector, λ = 0.154186 nm). The operating voltage of the X-ray tube was 40 kV and the current was 40 mA [65]. The measurement time for one step was 492 s. The scanning step 2θ was 0.01° (2θ from 10° to 90°). To determine the Pt lattice parameters and the size of the Pt crystallites, the catalyst diffractograms were modelled using the Topaz program. The XRD measurements were carried out by Mr Jaan Aruväli.

Thermogravimetric analysis was performed on the synthesised catalyst materials and the commercial catalyst to determine the platinum content. TGA was also performed on the carbon support materials of the catalyst materials to determine the amount of non-burning residue, or ash. Before and after measuring the samples, baselines were measured with an empty crucible. An aluminum oxide crucible was used for measurement. Since the temperature ramp rate and the gas flow rate affect the recorded TGA signal, the baselines must be measured. As the density of the gases decreases, the weight of the crucible increases at high temperatures. The agreement between the measured baselines was very good, with a maximum difference of 20 μg (significantly below the set criterion of 40 μg). After measuring the baselines, the sample was measured. TGA was performed using a NETZSCH STA 449 F3 Jupiter device. The mass of the measured sample was about 10 mg. The measurements were conducted in the temperature range from 25 °C to 1000 °C. The temperature was increased at a rate of 10 K min^{-1}. The following gas flow rates were used for the measurements: nitrogen (99.999%, AS Linde Gas) at 45 cm^3 min^{-1} and oxygen (99.999%, AS Linde Gas) at 5 cm^3 min^{-1}.

The low temperature nitrogen sorption measurements were performed with the 3Flex instrument (USA, Micromeritics). To remove moisture and gases from the pores of the samples, the samples were degassed (24 h, 100 °C, 0.05 mbar) before measurement. First, the samples were vacuumed and after that filled with nitrogen. While attached to the instrument, the samples were degassed again. During the measurement, the samples were in a container filled with liquid nitrogen (77 K). The analysis of the measurement results was performed using the SAIEUS software and the 2D-NLDFT-HS model. The assumption of the theory is that the adsorbing surface is heterogeneous energetically and in terms of pore structure. In addition, the specific surface area (S_{BET}) was calculated according to the BETtheory. The assumption of BET theory is that the adsorbing surface is energetically homogeneous and the adsorption energy is the same between different adsorbing layers. The total pore volume (V_{tot}) was calculated at a pressure close to the saturation pressure (pp_0^{-1} = 0.95).

2.3. Electrochemical Measurements

2.3.1. Preparation of Suspensions of Carbons and Catalysts

Measurements in the Three-Electrode System. A suspension of carbon or catalyst material for RDE measurements was prepared from the carbon or catalyst under investigation (5 mg), IPA (0.004 cm^3), Milli-Q$^+$ water (3 cm^3), and 1 M KOH aqueous solution (0.4 cm^3).[66] The required amount of starting materials was weighed and then the suspension was mixed for 15 min in an ultrasonic bath (37 kHz, 0 °C).

Measurements in the Two-Electrode System. To assemble and measure a PEMFC single cell, it is first necessary to prepare a suspension of the catalyst material [8]. For this purpose, the catalyst material under study was weighed in the glass vial (95,3 mg). Milli-Q$^+$ water (2.06 cm^3), IPA (4.64 cm^3) and Nafion solution (Nafion™ PFSA, Ion Power GmbH, ~5%) (0.83 cm^3) were added to the catalyst. The suspension was mixed for 15 min in an ultrasonic bath (37 kHz, 0 °C) and then mixed for 4 h at room temperature using a HIGH-SHEAR mixer (IKA ULTRA-TURRAX®; 14 600 rpm min^{-1}). After that, the suspension was left to stir with a magnetic stirrer overnight. Before applying the catalyst material to the GDL or membrane, the suspension was mixed again in an ultrasonic bath (15 min, 37 kHz, 0 °C) and with a HIGH-SHEAR mixer (14,600 rpm min^{-1}, 1 h).

In parentheses are given sample quantities for both recipes.

2.3.2. Rotating Disc Electrode Measurements

Prior to conducting the RDE measurement, the necessary glassware was subjected to acid washing using heated (80°C) H_2SO_4 (ACS Reagent, 95,0–98,0%, Sigma-Aldrich) with small addition of H_2O_2 (EMSURE, ISO, 30%) followed by thorough rinsing with demineralised water and Milli-Q$^+$ water.

The ORR activity of the catalysts was measured using the RDE method in 0.1 M $HClO_4$ (Suprapur, Sigma-Aldrich, 70%) aqueous solution. The solution was titrated to determine the exact concentration.

Before the suspension of the carbon material or catalyst under study was applied to the glassy carbon disc electrode (PINE Instrument Company, S = 0.196 cm^2), the electrodes were first polished with a paste containing alumina powder (BUEHLER Micro Polish) with a larger grain (0.3 μm) and then with a paste with a smaller grain (0.05 μm). The electrodes were then thoroughly rinsed by pouring Milli-Q$^+$ water over them and treated in Milli-Q$^+$ water in an ultrasonic bath (frequency 37 kHz, room temperature) for 15 seconds. The electrodes were allowed to dry under the flow of compressed air. The catalyst suspension was then pipetted as a single drop (9 μl) onto the electrode. The electrodes were dried for 30 min in the vapours of a mixture of IPA and Milli-Q$^+$ water (80% IPA : 20% H_2O) to get the uniform catalyst layer [66]. Afterwards, the electrodes were additionally dried for another 15 min in a drying cabinet at a temperature of 40 °C to get rid of the volatile organic matter. The loading of Pt was 54 μg_{Pt} cm^{-2} for the synthesised catalyst **S1** and 18 μg_{Pt} cm^{-2} for the other synthesised catalysts (**S2** and **S3**) and the commercial catalyst **K**. The loading of C was 37 μg cm^{-2} for the synthesised catalyst **S1** and 12 μg cm^{-2} for the other synthesised catalysts (**S2** and **S3**) and the commercial catalyst **K**.

Potentiostat (Metrohm, Autolab B. V., PGSTAT302N, FRA32M) and NOVA 1.10.4 software were used for the CV and RDE measurements. Before the measurement, the electrolyte solution was saturated with argon (99,9999%, AS Linde Gas). First, the working electrode was cycled in the potential range of 0.025-1.200 V. Next, electrochemical impedance spectroscopy (EIS) was measured at a potential of 450 mV in the frequency range of 0.1-10 000 Hz (5 mV_{rms}). The electrolyte resistance value, R_{el}, (between the working and reference electrodes) found from the EIS data was used to compensate for the ohmic potential drop during the CV and RDE measurements. After that, CV was measured at potentials from 0.02 V to 1.00 V and potential sweep rates from 10 mV s^{-1} to 400 mV s^{-1}. RDE measurements were performed at a rotation speed of 1600 rpm in an argon-saturated environment and then in an oxygen saturated environment in the potential range from −0.10 V to 1.00 V at a potential sweep rate of 20 mV s^{-1}.

A glassy carbon disc working electrode covered with the investigated material, a reversible hydrogen electrode (RHE, reference electrode [67]) and a large-surface area Pt mesh auxiliary electrode were used as electrodes. The reference electrode was connected to the system via a Luggin capillary. In the thesis, all electrode potentials are given against RHE. The measurements were carried out in a glass measuring cell.

2.3.3. Membrane Electrode Assembly Preparation

To make an MEA, the Nafion membrane must be coated on one side with an anode catalyst and on the other side with a cathode catalyst, and GDLs are placed on both sides. Sputtering is the traditional method for applying anode and cathode catalysts to the MEA with using special equipment such as ultrasonic spray system [68]. For coating, the Nafion membrane (5 cm^2, Nafion HP, Ion Power GmbH) was placed on a preheated plate (60 °C) in the ultrasonic spraying system (Sono-Tek ExactaCoat), and the anode material, which was a commercial catalyst **K**, was sprayed on top of it with a Pt loading of 0.5 mg cm^{-2}. In the same way, the other side of the membrane was covered with the commercial catalyst **K** with a Pt loading of 0.7 mg cm^{-2}. In the work, the resulting MEA is denoted as **K**.

An alternative approach was employed to fabricate MEAs using the synthesised catalyst materials (**S1**, **S2**, **S3**), as previous studies have indicated that catalysts where with platinum deposited on waste tire carbon are unsuitable for MEA production via the spray coating method [58]. Therefore, the anode side was prepared as before, but for the cathode, the catalyst material was pipetted onto the GDL (2.35×2.35 cm), (Freudenberg H24C3, FuelCellStore) in several drops. Pipetting the suspension onto the GDL took place on a stove heated to 80 °C, where the GDL was fixed with carbon tape. A total of 277 µl of the suspension was dropped onto the GDL in 10 µl drops. Pt loading on the cathode side was 0.7 mg cm^{-2} for all cases. Further processing of the MEA by adding an additional Nafion layer and subjecting the entire MEA to hot pressing is suggested in the literature to increase the power output of the PEMFC. [69]. The Nafion layer was applied using an ultrasonic spray system and MEA with GDLs was hot pressed using an A CARVER®. INC device (3 min, 250 kg, 125 °C). MEAs prepared in this way are denoted **S1**, **S2** and **S3** in the work.

2.3.4. PEMFC Unit Cell Experiments

Initially, all single cell components (end plates, current collectors, bipolar plates, Teflon gaskets) (Fuel Cell Store) were cleaned with ethanol (96.3%, Premium) followed by the assembly of single cells utilising MEAs prepared by different methods [70]. While assembling the single cell, the Teflon gaskets were sprayed with Milli-Q^+ water to ensure a gas tighter system. The components of the unit cell were fixed using nuts and bolts with a torque of 7 N m.

Measurements were performed using a potentiostat (PGSTAT302N, FRA32M, Autolab) with a booster (BOOSTER20A). The utilised equipment by FUEL CELL TECHNOLOGIES, INC facilitated precise control over gas flow rates at both the cathode and the anode, as well as the regulation of gas humidity, temperature, and pressure. During the measurement, the temperature of the gas lines was 60 °C and the temperature of the cell was 62 °C. Synthetic air (Airapy 100%, AS Linde Gas) was fed into the cell from the cathode side at a flow rate of 2 dm^3 min^{-1} at atmospheric pressure and hydrogen (99,999%, As Linde Gas) was fed into the cell from the anode side at a flow rate of 200 cm^3 min^{-1} and a pressure of 1.4 bar. The measurements were carried out in the galvanostatic mode, starting with the voltage measurement at a current of 0 A and finishing the measurements at a current at which the cell voltage was 0.4 V. The applied currents were: 0 A, −0.005 A, −0.05 A, −0.2 A; thereafter, the current was decreased by 0.2 A at each step. The measurement time was 30 s for the first three points and 60 s for the subsequent points . The electrochemical activity was evaluated at cell voltage of 700 mV and the open circuit voltage (OCV) and maximum power density (P_{max}) were determined. In the frequency range of 0.5-100 000 Hz, the resistance (R) was measured both in the galvanostatic (0.4 A cm^{-2}, 0.02 A_{rms}) mode and in the potentiostatic (−450 mV vs OCV, 0.005 V_{rms}) mode.

The next day, after the entire system (humidification vessels, gas lines and cell) had cooled down to room temperature, CV was performed in the potential range of 0.08-1.00 V vs. RHE at electrode potential sweep rates of 20–300 mV s^{-1}. Nitrogen was used at the cathode side at a pressure of 1 bar and a flow rate of 200 cm^3 min^{-1}, while hydrogen at a pressure of 1 bar and a flow rate of 12 cm^3 min^{-1} was used at the anode side. The CV data was used to calculate the ECA values.

2.4. Using artificial intelligence chatbots

Grammarly and Copilot artificial intelligence chatbots were used to check English grammar and sentence structure in the main text of the chapters. Based on the received feedback, the text of the work has been refined, and language errors have been corrected.

3. Results and Discussion

3.1. Physical Characterisation

3.1.1. Analysis of SEM and SEM-EDX Results

SEM and SEM-EDX analyses were performed on the carbon materials. SEM images (Figures 7 and 8) of all four investigated materials show that the carbons synthesised from waste tires are porous and inhomogeneous. Images at a magnification of 1000× (Figure 7) reveal distinct morphological differences. The first sample, **C1**, exhibits larger, irregularly shaped particles that are clumped together and form a rough surface. The particle size vary (there are both larger particles, a few tens of micrometers in diameter and smaller particles with a diameter of a few micrometers) but it is relatively large compared to the other samples. This could be due to the high pyrolysis temperature. In contrast, **C2** displays a smoother, more homogeneous surface with particles that are more difficult to distinguish, which might be due to the lower pyrolysis temperature. The third sample, **C3**, features well-defined yet smooth particles that aren't as clumped together as in **C1**, indicating the effect of KOH treatment. Lastly, **C4** exhibits a "smooth" surface but with some textural inconsistencies and lacks distinct structure characteristic of individual particles as those seen in other samples.

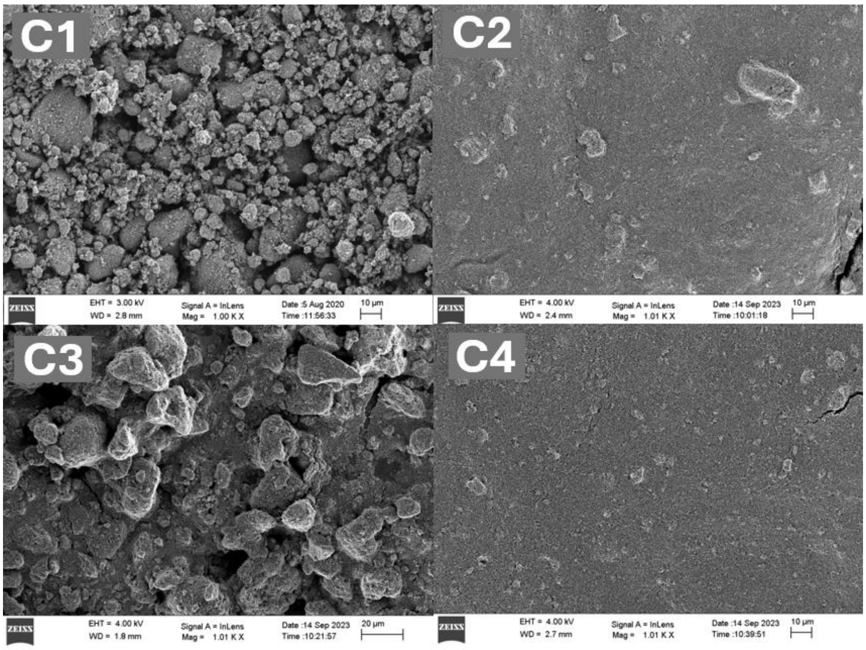

Figure 7. Scanning electron microscopy images of the waste derived carbons at 1 000× magnification.

At higher magnification (Figure 8), the morphologies of all carbon materials are very similar. The differences in preparation methods, such as pyrolysis temperatures, alkaline and acid treatment, ball milling, result in subtle variations in surface texture and particle distribution. However, these differences might not significantly alter the overall morphology. All the carbon materials are macroporous and contain voids.

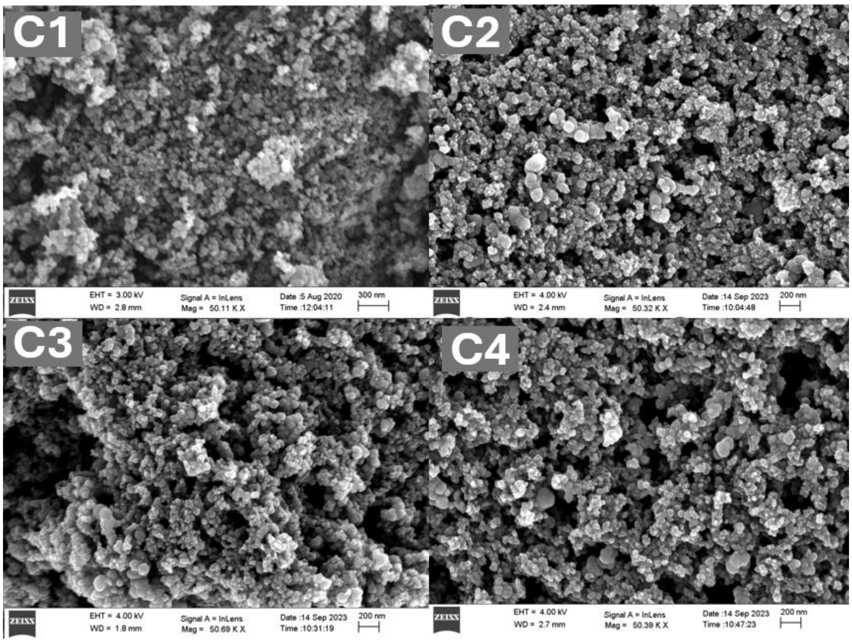

Figure 8. Scanning electron microscopy images of the waste derived carbons at 50 000× magnification.

Examining the elemental composition using the SEM-EDX method, it appeared (Table 1) that, as expected, all carbon materials consist mainly of carbon (70-88 wt%), oxygen (10-19 wt%) and some impurities like Zn (0.2-4.2 wt%), S (0.3-2.0 wt%) and a small amount of Al (0.1-0.2 wt%) and Ca. The content of Si, S, Ca and Zn is not surprising, because sulphur and zinc compounds are used to vulcanize rubber in tire production [71,72], and SiO_2 and $CaCO_3$ are used as fillers in tires [73,74]. Other authors have also observed a similar elemental content in residues after the pyrolysis of tires [75]. Since the **C1** material used to synthesise the Pt catalysts contained various impurities that could affect the electrochemical activity of the synthesised catalyst material, new carbons were produced [58]. The carbon **C2** has a very similar composition to **C1**, as the same batch of waste tire granules was used for pyrolysis, with only the pyrolysis temperature being different. The carbon **C3** underwent an alkaline treatment which reduced the Si amount; however, it is the only one that contains potassium (1.1 wt%) due to the KOH treatment. All three carbons (**C1**, **C2**, and **C3**) contain Ca, which **C4** does not have because HNO_3 treatment that helped eliminate it. Acid and alkaline treatment also significantly helped to reduce the amount of Zn (**C4** has only 0.2 wt%) and S (0.3 wt%). Therefore, the final carbon **C4** was used for the synthesis of the new Pt catalysts.

It should be stressed that SEM-EDX analysis results of porous carbonaceous materials are only semi-quantitative and provide some indication of the elemental composition of the studied materials.

Table 1. Scanning electron microscopy with energy dispersive X-ray analysis results for all carbon materials. Results are given as mass percent.

Material	C	O	Si	Zn	S	Ca	K	Other (< 0.5%)
C1	79	11	6.9	0.7	1.6	0.7	-	Mg, Al
C2	70	19	6.9	2.4	1.3	0.1	-	Al
C3	81	10	1.1	4.2	2.0	0.6	1.1	Mg, Al
C4	88	12	-	0.2	0.3	-	-	Cl, Al

3.1.2. X-ray Diffraction Analysis

XRD was performed on all the materials under studied (Figure 9). The carbon materials (Figure 9a) have clearly distinguishable carbon reflexes: C 002 and C 001/101 [76]. Since the carbon is amorphous, the reflexes are very broad. However, it can be clearly seen that for two materials **C1** and **C4** which were pyrolised at higher temperature (1000 and 700 °C, respectively) the C 002 peak is more pronounced and slightly sharper which can be associated with the formation on more graphitised carbon structure at higher temperatures. The clearly identifiable reflexes of ZnO, ZnS, $CaCO_3$, and SiO_2 in **C1**, **C2**, and **C3** suggest the presence of impurities as Si, Ca, and Zn. These impurities likely originate from the waste tire material used in the synthesis of carbon. The effectiveness of the acid and alkaline treatment is evident in the significantly reduced impurities observed in material **C4** as the reflexes of impurities are absent. This observation aligns with the findings from the SEM-EDX analysis (Table 1).

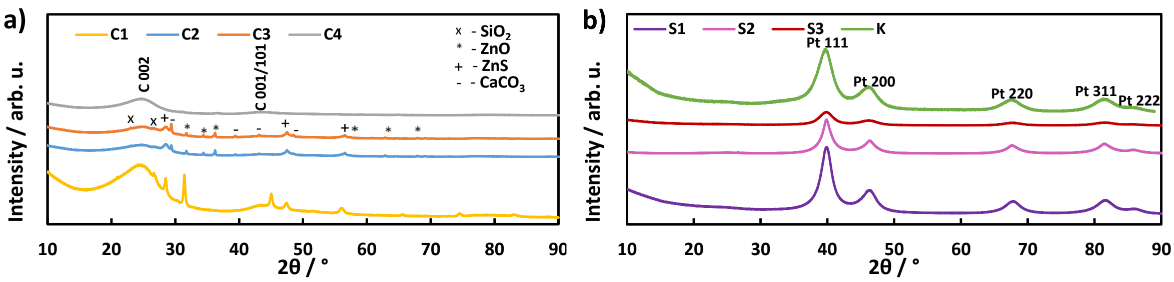

Figure 9. Diffractograms for **a)** all carbon materials and **b)** all catalysts.

The Pt catalysts were next investigated using the XRD. The Pt diffraction reflexes are visible in the diffractograms of the synthesised Pt catalyst materials (Figure 9b) [77], so we can conclude that the Pt deposition was successful. The lattice parameter, *a*, and the crystallite size, *d*, calculated from the data of XRD, are presented in Table 2. From the table, it is evident that the platinum crystallite size decreases in the sequence **S2** > **S1** > **S3** > **K**. By employing the second synthesis method, where Pt nanoparticles are initially synthesised and subsequently deposited on carbon, it appears feasible to synthesise a catalyst containing smaller Pt nanoparticles. Furthermore, it can be argued that the size of the Pt nanoparticle is almost independent of the carbon support used. The measured Pt lattice parameters of the catalysts align excellently with the platinum single crystal measurements given in the literature (a = 3.92 Å) [78].

Table 2. The Pt content of the investigated catalysts (in mass percent) from the results of thermogravimetry and the lattice parameter, *a*, and the crystallite size, *d*, from the data of X-ray diffraction analysis.

Material	**Pt content / %**	***a* / Å**	***d* / nm**
S1	56.0	3,915±0,014	2,8
S2	49.4	3,918±0,003	3,1
S3	56.9	3917±0,013	2,4
K	58.8	3,906±0,007	1,9

3.1.3. Thermogravimetric Analysis

TGA analysis was conducted on the materials under investigation (Figure 10). From the Figure 10a, it is evident that the oxidation of carbon starts approximately at 400 °C. The waste tire derived carbons are not fully oxidised, leaving behind a non-combustible residue, commonly referred as ash. These residues could be oxides or salts originating from the initial waste tire granules [79]. Material **C1** composed of 81.6% carbon and 18.4% non-combustible residue. [58]. The material **C4** appears to be the cleanest, i.e., it has the smallest ash residue (2.5% non-combustible residue). Material **C2** had the largest ash residue (23.2%), which is due to the fact that this material has been pyrolyzed once at 450 °C, such a low pyrolysis temperature does not allow more impurities to be removed. In addition to pyrolysis at 450 °C, material **C3** has also been washed with KOH, it has partially removed impurities, the ash residue is smaller (15.0%). Indeed, the acid and alkaline treatment played a crucial role in producing a nearly pure carbon material with minimal residue. TGA results align with the SEM-EDX analysis (Table 1) and XRD results (Figure 9).

In addition, the figure shows that carbons **C1** and **C4**, which have a higher pyrolysis temperature (1000 °C and 700 °C respectively), begin to oxidize at a higher temperature because the carbon structure is more graphitic.

In contrast to carbons, catalysts containing Pt begin to oxidise at lower temperatures. This indicates that Pt nanoparticles lower the oxidation temperature, acting as Pt catalyst for the oxidation reaction.

When determining the Pt content in the synthesised Pt catalysts, the non-combustible carbon residue was also taken into account. Therefore, after the catalyst is measured, Pt remains along with impurities from the carbon substrate that were not oxidised.

The calculation reveal that the Pt content in materials **S1** and **S3** is quite similar (56.0% and 56.9%, respectively). However, the Pt content in catalyst **S2** (49.4%) is slightly lower than expected (Table 2). The Pt content in the commercial catalyst **K** was determined as 58.8% (Table 2). This slightly lower value than nominal (60%) may be attributed to the absorption of atmospheric moisture.

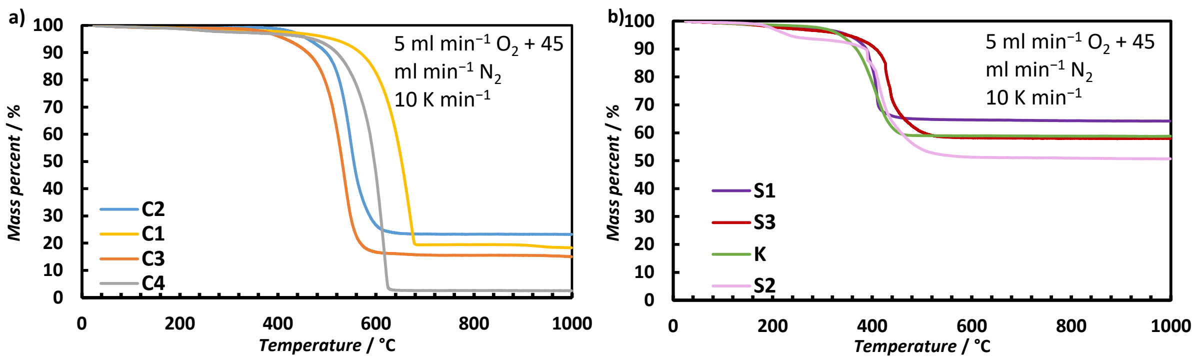

Figure 10. Thermogravimetric analysis results for **a)** the carbons and **b)** catalyst materials.

3.1.4. Nitrogen Sorption Analysis

Low-temperature N_2 sorption analysis was used to estimate the micro- and mesoporosity of the studied materials. The specific surface area values of the Pt catalysts and carbons are given in Table 3.

The table indicates that among waste tire carbon materials, **C1** has the highest specific surface area and pore volume according to both BET and DFT model. **C2** and **C3** have lower specific surface areas compared to **C4**, which has undergone repeated pyrolysis at higher temperature and acid and alkaline treatment. Additionally, the V_{micro}/V_{DFT} (the proportion of micropores in the material) increases in the order **C2** ≲ **C3** < **C1** ≲ **C4**. In summary, carbon **C4** has a smaller specific surface area and total pore volume compared to carbon **C1**; however, the relative proportion of micropores is very similar.

If we compare waste tire carbons **C1-C4** with commercial carbon (Ketjenblack, FuelCellStore), the specific surface area and total pore volume (according to both the BET and

DFT models) are significantly larger in the case of the commercial material. The other porosity parameters are also significantly higher. [58]

Table 3. Results of N_2 sorption analysis of the studied materials.

Material	S_{BET} m² g⁻¹	S_{DFT} m² g⁻¹	S_{micro} m² g⁻¹	V_{tot} cm³ g⁻¹	V_{DFT} cm³ g⁻¹	V_{micro} cm³ g⁻¹	V_{micro}/V_{DFT}
C1	125	116	73	0.27	0.23	0.03	0.13
C2	69	47	19	0.19	0.17	0.01	0.07
C3	59	40	16	0.16	0.14	0.01	0.08
C4	92	76	45	0.17	0.16	0.02	0.14
S1	74	72	49	0.13	0.12	0.02	0.16
S2	23	14	14	0.05	0.03	0.01	0.23
S3	41	26	35	0.06	0.06	0.01	0.19
K	328	308	239	0.36	0.33	0.10	0.30

S_{BET} – specific surface area according to the BET theory;
S_{DFT} –specific surface area according to the DFT model;
V_{tot} – total pore volume of material; V_{DFT} – total pore volume according to the DFT model;
V_{micro} – volume of micropores; V_{micro}/V_{DFT} – relative proportion of micropores.

The graphs of the pore size distribution (Figure 11) show that the carbon materials and catalyst materials are all micro-mesoporous. From the pore size distribution graph (Figure 11a), it can be also seen that materials **C2** and **C3** have a very similar pore size distribution, so KOH treatment does not affect the pore size distribution.

For all four catalysts (**S1**, **S2**, **S3** and **K**), a decrease in the specific surface area and pore volume (compared to the carbon support materials) can be observed, which is mainly due to a decrease in the proportion of carbon, because Pt particles contribute significantly less to the specific surface area than carbon.

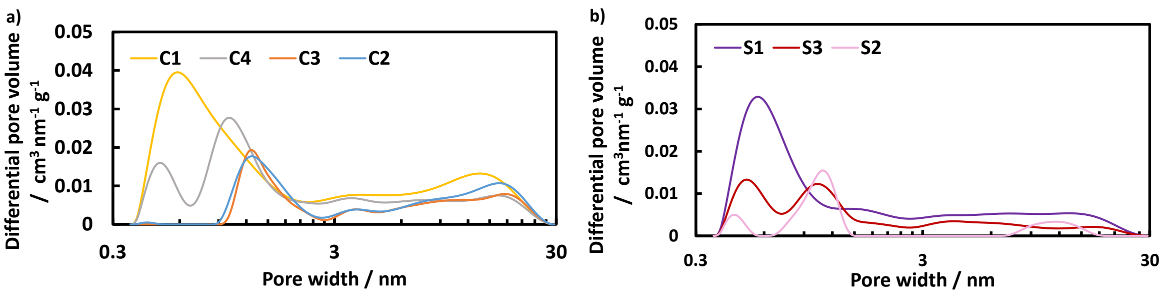

Figure 11. Pore size distributions of **a)** waste tire carbons and **b)** catalyst materials.

3.2. Electrochemical Characterisation

3.2.1. Carbon Supports

ORR was studied for all materials using RDE and CV methods. All RDE current density values in the work are corrected to the current densities measured in a solution saturated with argon or hydrogen. First, oxygen reduction was investigated on carbon material **C4** at different rotation speeds in 0.1 M $HClO_4$ solution saturated with oxygen (Figure 12a). The anode direction of the *j, E*-curves of the **C4** material can be seen in the figure. The potential sweep direction is marked by the arrow in the figure.

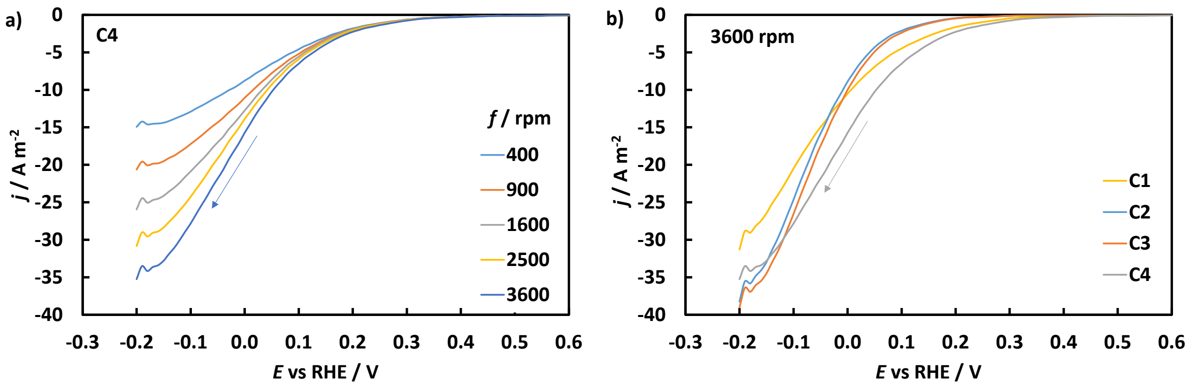

Figure 12. Dependence of current density, *j*, on electrode potential, *E*, **a)** at different electrode rotation speeds for material **C4** and **b)** for all carbon materials at 3600 rpm (0.1 V s^{-1}) in 0.1 M $HClO_4$ solution saturated with oxygen.

Three regions are usually distinguished on RDE voltammograms: the charge transfer region, the mixed kinetics region, and the region limited by mass transport. The current density in the region, where the kinetics is limited by the slow charge transfer, does not depend on the electrode rotation speed (for **C4**, E > 0.2 V vs RHE). In the region of mixed kinetics, the electrochemical process is limited by the slowness of the charge transfer and mass transport. In the mass transport-limited region, the reaction rate is influenced only by mass transport, so the current density does not depend on the electrode potential, but rather on the speed of rotation of the electrode.[45,50] For carbon materials under study, the mass transport-limited region has not developed, because at electrode potentials −0.2 V < E < −0.1 V vs RHE, the current density depends on both the electrode rotation speed and the electrode potential. Carbon materials synthesised from waste tires that have not developed a mass transport-limited plateau, have also been mentioned in the literature [80].

Figure 12b shows the dependence of the current density on the electrode potential for all carbon materials at the rotation rate of 3600 rpm in 0.1 M $HClO_4$ solution saturated with oxygen. It can be seen from this figure and Table 4 that the most active material is carbon **C4** with onset potential (E_{onset}) value of 0.28 V vs RHE. The E_{onset} potential indicates the potential value from which the ORR rate starts to increase significantly, taken at the current density $j = -1.0$ A m^{-2} [81]. Consequently, acid and alkaline treatment of initial carbon material increased the ORR activity of material **C4**. The next most active material is **C1** (E_{onset} = 0.24 V vs RHE), followed by **C2** and **C3** with very similar activities, with the E_{onset} values of 0.15 and 0.16 V vs RHE, respectively, suggesting these last two carbon materials have even lower activity for ORR. Therefore, carbons **C1** and **C4** were used in the synthesis of catalysts as support materials.

Table 4. Electrode potentials corresponding to current density −1 Am^{-2}, calculated number of transferred electrons, and Tafel slopes for all four carbon materials. Measured in 0.1 M $HClO_4$ solution, saturated with oxygen.

Material	E_{onset} / V vs RHE @ j= −1 Am^{-2}	n @ −0.1 V vs RHE	Tafel slope / mV dec^{-1}
C1	0.24±0.01	2.01±0.02	221±1
C2	0.15±0.01	1.98±0.02	153±3
C3	0.16±0.01	2.00±0.02	148±3
C4	0.28±0.01	1.95±0.02	219±1

Koutecký-Levich dependencies were established for all materials, enabling the calculation of the number of electrons transferred per oxygen molecule, n, depicted in Figure 13a. Based on Figure 13a and Table 4, it is evident that the value of n is around two for all carbon materials derived from waste tires in the mixed kinetics region. This is characteristic to a carbon-specific two-electron process where oxygen is reduced to hydrogen peroxide [50].

$$O_2 + 2H^+ + 2\,e^- \rightarrow H_2O_2 \quad (11)$$

The Tafel dependences (Figure 13b), or E, log($-j_k$) dependences, were constructed based on the values of the kinetic current densities derived from the Koutecký-Levich dependences (Eq. 10) constructed in the potential region of mixed kinetics. The values of the Tafel slope found in the linear part of the dependencies are given in Table 4. It can be seen that two carbon materials pyrolysed at high temperatures, namely **C1** and **C4**, with a more graphitised structure (Figure 9a) exhibit closely comparable slope values (220±1 mV dec^{-1}), whereas materials **C2** and **C3** demonstrate slightly lower values (150±3 mV dec^{-1}). These high Tafel slope values are not unusual in neutral and acidic solutions [82,83]. Therefore, the ORR mechanism for carbons with similar a structure seems to be similar.

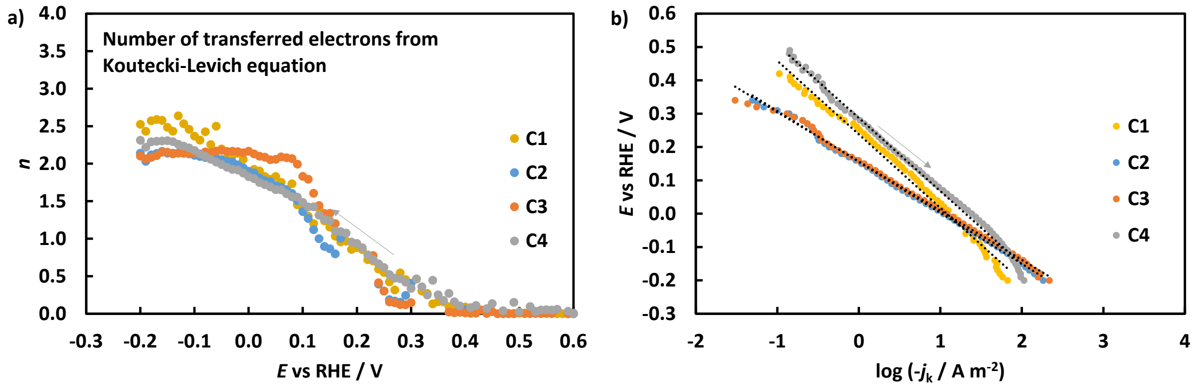

Figure 13. a) Dependence of the number of electrons transferred in the reaction on the electrode potential, and **b)** Tafel plots for all carbon support materials. Measured in 0.1 M $HClO_4$ solution and saturated with oxygen.

3.2.2. Catalyst Materials

Next, the RDE experiments in 0.1 M $HClO_4$ solution saturated with oxygen were performed on the catalyst materials at one rotation speed (1600 rpm). By using Koutecký-Levich formula (Eq. 10), it was found that the number of electrons transferred per oxygen molecule is four for catalysts **S1**, **S2** and **K**, which corresponds to a 4-electron process, i.e. the reduction of oxygen to water (Eq. 2) [84]. However, for the catalyst **S3** the value of n is slightly below four indicating partial formation hydrogen peroxide or the catalyst layer was not uniform enough. j, E-dependencies for the catalyst materials are shown in Fig. 14a. From Figure 14a, it can be seen that at potential values $E < 0.65$ V for materials **S1**, **S2** and **K**, the measured current density values are close to the theoretical diffusion-limited current density value calculated from Levich equation (Eq. 9) ($j_{D,theor} = -59.8$ A m^{-2} for $n = 4$) and at the given potentials, the reduction of oxygen is limited by mass transport. In the case of material **S3**, the value of the diffusion-limited current density was not reached, and the ORR activity is also significantly lower, which may come also from the uneven coating of the material on the glassy carbon electrode [47]. To compare the charge transfer kinetics of the materials, the Tafel dependences are constructed (Figure 14b). The values of the Tafel slope found are in the range of 53-66 mV (Table 5) and show no substantial reliance on the catalyst when it comes to areas of low current densities, denoted as $|j_c|$ (where the potential range is 0.90…1.00 V vs. RHE). These results are in good agreement with the materials presented in the literature [85].

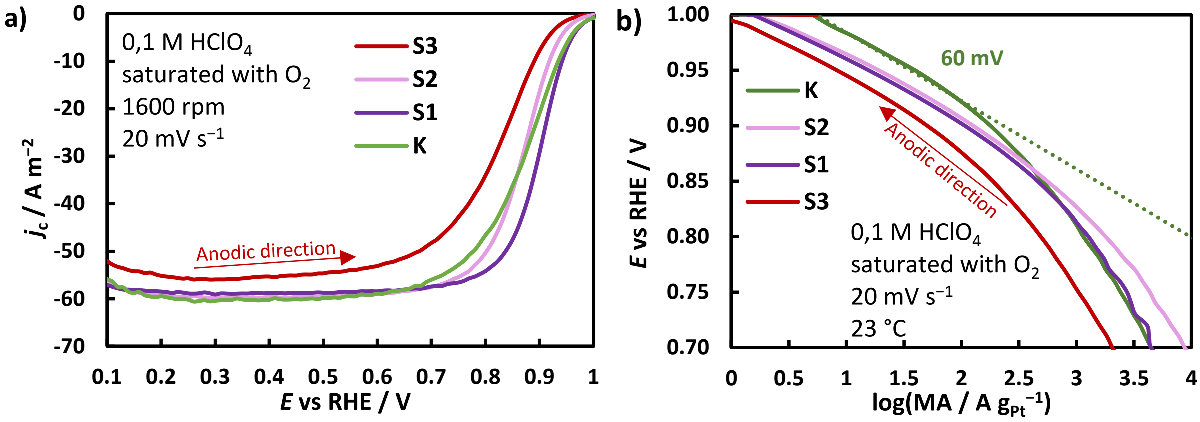

Figure 14. a) j, E-dependences and **b)** Tafel dependences of the studied catalysts.

The mass activity (MA) and specific activity (SA) of the catalysts were determined at an electrode potential of 0.9 V vs RHE (Table 5). MA (A g_{Pt}^{-1}) was computed by dividing the kinetic current density by the surface concentration of Pt, while SA (A m_{Pt}^{-2}) was calculated by dividing the kinetic current by the ECA of Pt nanoparticles in square meters. [86]. The MA of catalyst materials increases in the order of catalysts **S3** < **S1** ≲ **S2** < **K**. A higher MA value is associated with a better dispersibility of platinum on the support material. The values of SA for materials **S1**, **S3** and **K** are relatively similar to each other, slightly higher in the case of **S2**. However, it is worth highlighting that the surface concentration of material **S1** is three times higher than for the other materials.

Table 5. Electrochemically active surface area (ECA) and oxygen reduction activity parameters of Pt-based catalyst materials in 0.1 M $HClO_4$ solution saturated with argon.

Materjal	**ECA / m_{Pt}^2 g^{-1}_{Pt}**	**j_D / A m^{-2}**	**MA / A g_{Pt}^{-1} @ 0.9 V vs RHE**	**SA / A m_{Pt}^{-2} @ 0.9 V vs RHE**	**Tafel slope / mV dec^{-1}**	**Pt loading / μg_{Pt} cm^{-2}**
S1	26.6	−58.8	107	4.0	54	54
S2	19.2	−59.6	112	5.8	53	18
S3	16.1	−55.5	53	3.3	56	18
K	56.6	−60.2	179	3.2	62	18

j_D – diffusion-limited current density; MA – mass activity; SA – specific activity. The Tafel slope value is found in the range of electrode potentials from 0.90 to 1.00 V vs RHE.

To evaluate ECA, CV measurements were performed in a 0.1 M $HClO_4$ solution saturated with argon, and the C, E-dependencies are presented in Figure 15. From the cyclic voltammograms, hydrogen and oxygen ads/des regions can be clearly distinguished ($E < 0.38$ V and $E > 0.65$ V vs RHE, respectively). Since Pt nanoparticles are very well-dispersed in the commercial material, it is evident that material K possesses the highest gravimetric capacity and displays the most distinct hydrogen ads/des peaks. In the EDL region (0.40 V < E < 0.65 V vs RHE), all synthesised materials (**S1**, **S2** and **S3**) have similar capacitances. The commercial material has a significantly higher gravimetric capacitance in the EDL region because it also has much higher specific surface area (Table 3) than other catalysts. ECA values of the catalysts (Table 5) determined by the method outlined in Chapter 1.5.1. demonstrate that ECA values increase in an order of materials **S3** < **S2** < **S1** < **K**. Generally, a smaller Pt crystallite within the materials (Table 2) correlates with a higher ECA value. However, material **S3**, despite having the smallest Pt crystallite size (as determined by XRD), exhibits the smallest ECA value. This discrepancy may arise from the agglomeration of Pt nanoparticles in the material, thereby resulting in a low ECA value. If one compares the ECA and MA values of tire derived carbon given in the literature, the values in this work are significantly higher: the highest ECA value of tire carbon obtained in the literature is 13.2 $m_{Pt}^2\ g^{-1}{}_{Pt}$ and the highest mass activity value is 0.055 $A\ g_{Pt}^{-1}$ [21].

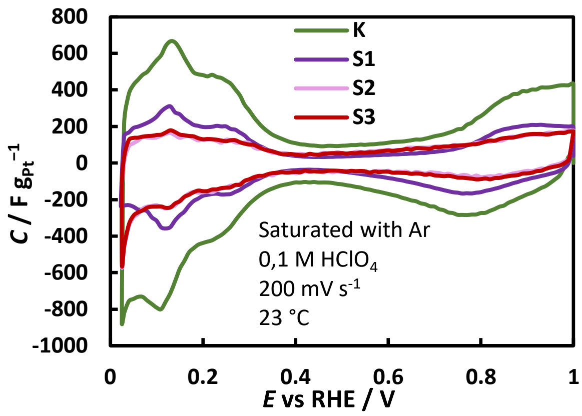

Figure 15. Dependence of the gravimetric capacitance of the catalyst materials under study on the electrode potential in a three-electrode system.

3.2.3. PEMFC Measurements

From the synthesised catalysts **S1**, **S2** and **S3** cathode layer of the PEMFC single cell was prepared by pipetting the suspension onto the GDL, to which an additional Nafion layer was added, and the completed MEA was hot-pressed. Using the commercial catalyst K as the cathode catalyst, a suspension was prepared and sprayed onto the Nafion membrane. The optimal preparation methods of MEAs were based on previous work, where it was found that the application of catalyst on the Nafion membrane is not suitable for synthesised catalysts based on waste tire carbon and vice versa, that commercial catalyst is not suitable for coating on GDL [58]. Since the synthesised catalysts (**S1**, **S2**, **S3**) and the commercial catalyst **K** are so different in terms of physical parameters, different methods of MEA preparation are also suitable for them. In the case of synthesised catalysts, if the suspension is sprayed on the membrane, probably a too dense layer is obtained, making the mass transport of reactants difficult in the catalyst layer. However, by applying the suspension to the GDL, the necessary transport porosity is preserved, which promotes the mobility of gases in the catalyst layer and avoids the condensation of water. The results of the PEMFC single cell experiments with prepared MEAs are shown in Figure 16a. The figure illustrates that the highest power density is achieved using a commercial catalyst as cathode material with a maximum power density of 0.63 W cm^{-2}. Additionally, the current density for commercial catalyst was also the highest, reaching 0.46 A cm^{-2} at potential 0.7 V (Table 6). The excellent performance of the PEMFC single cell containing the commercial material can be attributed to the small size of the Pt crystallites (Table 2), high ECA and the best match of the physical properties of the carbon used as the support material. In terms of maximum power density (P_{max}), the sequence of synthesised catalysts is as follows: **S1** > **S2** > **S3** and P_{max} values achieved are 0.42, 0.40 and 0.29 W cm^{-2}, respectively (Table 6). From Table 6, we can see that for three synthesised catalysts, the current density at 0.7 V is highest for the material **S1**, reaching 0.35 A cm^{-2}, and for the other two catalyst materials (**S2** and **S3**), this value is same and about two times lower, i.e. 0.12 A cm^{-2}.

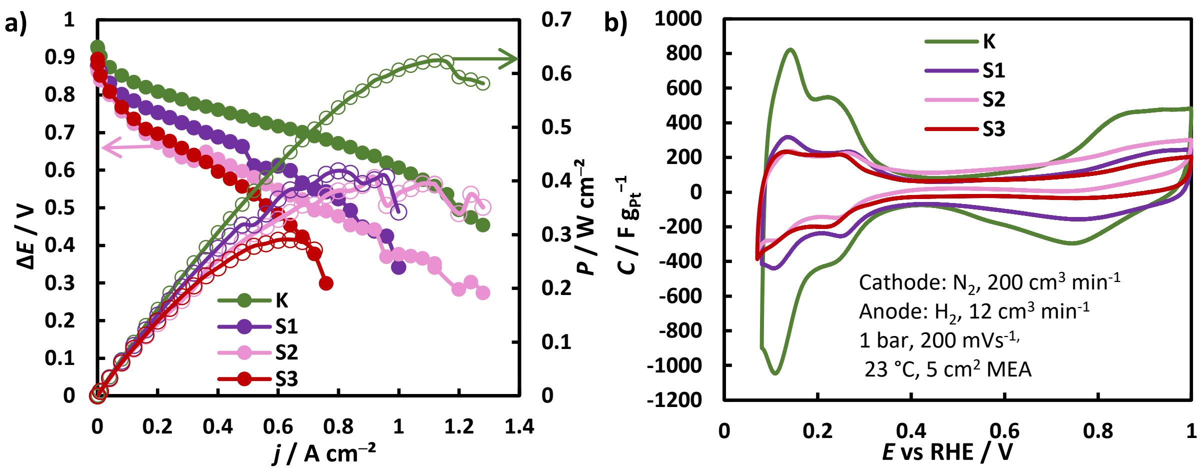

Figure 16. The results of measurements of a 5 cm^2 PEMFC single cell (H_2|air element) of the studied catalyst materials: **a)** dependence of cell voltage and power density on current density and **b)** dependence of gravimetric capacitance on the electrode potential. Cell temperature: 62 °C; temperature of humidification vessels and gas lines: 60 °C; cathode: air 1 bar 2 dm^3 min^{-1}; anode: H_2 1.4bar 200 cm^3 min^{-1}; catalyst loadings of cathode and anode: 0.7 mg cm^{-2} and 0.5 mg cm^{-2}, respectively.

Figure 16b shows the dependence of the gravimetric capacitance on the electrode potential for these MEAs. The ECA values were determined using the calculation method described in Chapter 1.5.1. and are presented in Table 6. The figure and calculations show that ECA value decreases in order: **K** > **S1** > **S3** ≈ **S2** (Table 6). These ECA values calculated from MEAs measurements are in agreement with results obtained from CV measurements in 0.1 M $HClO_4$ solution (Figure 15 and Table 5). Consequently, the CVs measured in the three-electrode system give a very good overview of ECA of Pt nanoparticles, and the behaviour of the material can already be predicted to a certain extent when measuring the PEMFC single cell, because in general, the higher the ECA value, the better the cell performance.

Table 6. The results of the measurements of the 5 cm^2 PEMFC single cell (H_2|air element) of the investigated materials. Cell temperature: 62 ℃; temperature of humidification vessels and gas lines: 60 ℃; cathode: air 1 bar 2 $dm^3\ min^{-1}$; anode: H_2 1.4 bar 200 $cm^3\ min^{-1}$; catalyst loadings of cathode and anode: 0.7 mg cm^{-2} and 0.5 mg cm^{-2}, respectively.

Material	*ECA* / $m_{Pt}^2\ g_{Pt}^{-1}$	*OCV* / mV	j / A cm^{-2} @ 700 mV	P_{max} / W cm^{-2}	R / mΩ @0.4 A cm^{-2}	R / mΩ @−450 mV vs OCV
S1	30	888	0.35	0.42	12	11
S2	18	842	0.12	0.40	14	16
S3	18	876	0.12	0.29	16	17
K	56	990	0.46	0.63	12	13

In conclusion, the most active synthesised material was **S1**, which was synthesised using tire derived carbon (**C1**) as a support material. This carbon contained more impurities compared to **C4**, which was used in the synthesis of the **S2** material. Both catalysts (**S1** and **S2**) are synthesised using the same method: Pt nanoparticles are deposited onto carbon from a solution, with the solution's temperature gradually increased to the synthesis temperature of 110 ℃. The better performance of **S1** in PEMFC single cell may be due to the fact that it has the highest specific surface area of all synthesised catalysts and the **C1** used as its support carbon material is the most mesoporous. The synthesis of the **S3** material used the same carbon support as in the case of **S2**, but different Pt deposition method was used where Pt nanoparticles were first synthesised in a preheated oil bath at 160 ℃ and then by using a rotary evaporator the Pt particles were deposited on the carbon. By comparing the maximum power density values (Table 6) for different catalysts (high current density region), we can conclude that while the support material influences the Pt catalyst's final ORR activity, its impact is relatively minor. The synthesis method, specifically how Pt is deposited on carbon, plays a significantly larger role. However, it is important to look at the kinetic part at low current densities where fuel cells actually work [87]. In this region, **S1** material also has the best performance among the three synthesised catalysts and the behaviour of the other two catalyst materials (**S2** and **S3**) is similar indicating that the physical properties of the carbon support used to play a significant role in this region and the Pt deposition method is not so important. Interestingly, among the synthesised materials, **S3** synthesis has the highest Pt content and the smallest Pt crystallite size, but in electrochemical characterisation, this material gives the lowest activity and ECA value. This is because the small Pt particles agglomerate during the synthesis. Usually the smaller the particle, the better the performance of the cell. [88]

In each measurement, the commercial material was the best, followed by the synthesised materials. Thus, ways should be found to increase the activity of the synthesised materials and optimise the preparation of MEA. One possible solution would be to change the synthesis conditions of the catalyst materials, for example by changing the ratio of the reactants used. By modifying carbon synthesis method and optimizing the catalyst synthesis method, it is possible to synthesise even more active Pt catalyst materials, with which to achieve results close to the commercial material.

Summary

In this study, four carbon materials and three Pt catalysts were investigated using different physical and electrochemical characterisation methods. Since the initial carbon obtained from the waste tires (**C1**) contained some impurities, the carbon synthesis procedure was modified and acid and alkaline treatment were included. SEM-EDX, TGA and XRD analysis revealed that modified carbon **C4** contained significantly fewer impurities compared to carbon **C1**, meaning that many impurities can be removed by acid and alkaline treatment. Using these two carbons, Pt catalysts (**S1** and **S2**, respectively) were synthesised by depositing Pt nanoparticles from a synthesis solution onto the carbon, with the reaction mixture's temperature gradually increasing to the final synthesis temperature of 110 ℃. The synthesis of the third Pt catalyst (**S3**) utilised carbon (**C4**) with fewer impurities and with a lower specific surface area (according to N_2 sorption analysis). A different Pt deposition method was used for this catalyst (**S3**) - the Pt nanoparticles were pre-synthesised in a preheated oil bath at 160 ℃, and then by using a rotary evaporator, the Pt nanoparticles were deposited on carbon.

The sizes of Pt crystallites (determined from XRD) for catalyst materials increased in the series **K** < **S3** < **S1** < **S2** being 1.9 nm, 2.4 nm, 2.8 nm and 3.1 nm, respectively. The results of the N_2 sorption analysis revealed that the specific surface areas of the synthesised catalysts were considerably smaller than those of the commercial materials and all catalysts were micro-mesoporous.

ORR activity was studied for all materials in 0.1 M $HClO_4$ solution using RDE and CV methods. It was found that the most active carbon material is **C4** with the onset potential value of 0.28 V vs RHE, while the onset potential of **C1** material is 40 mV more negative. Consequently, acid and alkaline treatment increased the ORR activity of carbon. Moving on to the electrochemical properties of catalyst materials. The ECA values found in a three-electrode system increase in the series **S3** (16.1 m_{Pt}^2 g^{-1}_{Pt}) < **S2** (19.2 m_{Pt}^2 g^{-1}_{Pt}) < **S1** (26.6 m_{Pt}^2 g^{-1}_{Pt}) < **K** (56.6 m_{Pt}^2 g^{-1}_{Pt}). The ECA values measured in the PEMFC experiment increase in the same order. Generally, a higher ECA ensures excellent performance of the material in PEMFC single cells. This also applies to the materials investigated, where commercial material has the best performance. PEMFC experiments revealed that material **S1** had the highest maximum power density (0.42 W cm^{-2}) and also had the highest current density at 0.7 V (0.35 A cm^{-2}) among the synthesised catalysts, although material **C1** with the highest amount of impurities was used as the support carbon for this material.

The synthesised materials are very different from the commercial ones in terms of physical parameters and are less active towards ORR. Therefore, the Pt deposition conditions should be optimised and carbon synthesis method should be modified in the future to increase the activity of the catalyst material.

References

[1] S. Bouckaert, A.F. Pales, C. McGlade, U. Remme, B. Wanner, L. Varro, D. D'Ambrosio, T. Spencer, Net Zero by 2050: A Roadmap for the Global Energy Sector, (2021). https://trid.trb.org/View/1856381 (accessed February 7, 2024).

[2] M.Z. Jacobson, M.A. Delucchi, Z.A.F. Bauer, S.C. Goodman, W.E. Chapman, M.A. Cameron, C. Bozonnat, L. Chobadi, H.A. Clonts, P. Enevoldsen, J.R. Erwin, S.N. Fobi, O.K. Goldstrom, E.M. Hennessy, J. Liu, J. Lo, C.B. Meyer, S.B. Morris, K.R. Moy, P.L. O'Neill, I. Petkov, S. Redfern, R. Schucker, M.A. Sontag, J. Wang, E. Weiner, A.S. Yachanin, 100% Clean and Renewable Wind, Water, and Sunlight All-Sector Energy Roadmaps for 139 Countries of the World, Joule 1 (2017) 108–121. https://doi.org/10.1016/j.joule.2017.07.005.

[3] S. Singh, S. Jain, V. Ps, A.K. Tiwari, M.R. Nouni, J.K. Pandey, S. Goel, Hydrogen: A sustainable fuel for future of the transport sector, Renew. Sust. Energ. Rev. 51 (2015) 623–633. https://doi.org/10.1016/j.rser.2015.06.040.

[4] A.Z. Weber, S. Balasubramanian, P.K. Das, Proton Exchange Membrane Fuel Cells, in: K. Sundmacher (Ed.), Advances in Chemical Engineering, Academic Press, 2012: pp. 65–144. https://doi.org/10.1016/B978-0-12-386874-9.00003-8.

[5] P. Grammelis, N. Margaritis, P. Dallas, D. Rakopoulos, G. Mavrias, A Review on Management of End of Life Tires (ELTs) and Alternative Uses of Textile Fibers, Energies 14 (2021) 571. https://doi.org/10.3390/en14030571.

[6] G.-S. Kang, G. Lee, S.Y. Cho, H.-I. Joh, D.C. Lee, S. Lee, Recycling of waste tires by synthesizing N-doped carbon-based catalysts for oxygen reduction reaction, Appl. Surf. Sci. 548 (2021) 149027. https://doi.org/10.1016/j.apsusc.2021.149027.

[7] H. Nagamoto, Fuel Cells: Electrochemical Reactions, in: K.H.J. Buschow, R.W. Cahn, M.C. Flemings, B. Ilschner, E.J. Kramer, S. Mahajan, P. Veyssière (Eds.), Encyclopedia of Materials: Science and Technology, Elsevier, Oxford, 2001: pp. 3359–3367. https://doi.org/10.1016/B0-08-043152-6/00600-8.

[8] D.S. Kim, C. Welch, R.P. Hjelm, Y.S. Kim, M.D. Guiver, Polymers in Membrane Electrode Assemblies, in: K. Matyjaszewski, M. Möller (Eds.), Polymer Science: A Comprehensive Reference, Elsevier, Amsterdam, 2012: pp. 691–720. https://doi.org/10.1016/B978-0-444-53349-4.00287-9.

[9] G. Squadrito, Preparation of MEA, in: V. Hacker, S. Mitsushima (Eds.), Fuel Cells and Hydrogen, Elsevier, 2018: pp. 117–138. https://doi.org/10.1016/B978-0-12-811459-9.00006-2.

[10] M. Shao, Q. Chang, J.-P. Dodelet, R. Chenitz, Recent Advances in Electrocatalysts for Oxygen Reduction Reaction, Chem. Rev. 116 (2016) 3594–3657. https://doi.org/10.1021/acs.chemrev.5b00462.

[11] C. Chen, Y. Kang, Z. Huo, Z. Zhu, W. Huang, H.L. Xin, J.D. Snyder, D. Li, J.A. Herron, M. Mavrikakis, M. Chi, K.L. More, Y. Li, N.M. Markovic, G.A. Somorjai, P. Yang, V.R. Stamenkovic, Highly crystalline multimetallic nanoframes with three-dimensional

electrocatalytic surfaces, Science 343 (2014) 1339–1343. https://doi.org/10.1126/science.1249061.
[12] M. Gurz, E. Baltacioglu, Y. Hames, K. Kaya, The meeting of hydrogen and automotive: A review, Int. J. Hydrogen Energ. 42 (2017) 23334–23346. https://doi.org/10.1016/j.ijhydene.2017.02.124.
[13] X. Zhang, H. Li, J. Yang, Y. Lei, C. Wang, J. Wang, Y. Tang, Z. Mao, Recent advances in Pt-based electrocatalysts for PEMFCs, RSC Adv. 11 (2021) 13316–13328. https://doi.org/10.1039/D0RA05468B.
[14] L. Du, G. Zhang, S. Sun, Proton Exchange Membrane (PEM) Fuel Cells with Platinum Group Metal (PGM)-Free Cathode, Automot. Innov. 4 (2021) 131–143. https://doi.org/10.1007/s42154-021-00146-0.
[15] L. Mølmen, K. Eiler, L. Fast, P. Leisner, E. Pellicer, Recent advances in catalyst materials for proton exchange membrane fuel cells, APL Mater. 9 (2021) 040702. https://doi.org/10.1063/5.0045801.
[16] R. Othman, A.L. Dicks, Z. Zhu, Non precious metal catalysts for the PEM fuel cell cathode, Int. J. Hydrogen Energ. 37 (2012) 357–372. https://doi.org/10.1016/j.ijhydene.2011.08.095.
[17] P.C. Okonkwo, O.O. Ige, E.M. Barhoumi, P.C. Uzoma, W. Emori, A. Benamor, A.M. Abdullah, Platinum degradation mechanisms in proton exchange membrane fuel cell (PEMFC) system: A review, Int. J. Hydrogen Energ. 46 (2021) 15850–15865. https://doi.org/10.1016/j.ijhydene.2021.02.078.
[18] G. Wang, W. Zhao, M. Mansoor, Y. Liu, X. Wang, K. Zhang, C. Xiao, Q. Liu, L. Mao, M. Wang, H. Lv, Recent Progress in Using Mesoporous Carbon Materials as Catalyst Support for Proton Exchange Membrane Fuel Cells, Nanomaterials 13 (2023) 2818. https://doi.org/10.3390/nano13212818.
[19] D.K. Madheswaran, P. Thangavelu, R. Krishna, M. Thangamuthu, A. Joseph Chandran, I. Colak, Carbon-based materials in proton exchange membrane fuel cells: a critical review on performance and application, Carbon Lett. 33 (2023) 1495–1518. https://doi.org/10.1007/s42823-023-00526-y.
[20] D. Banham, F. Feng, T. Fürstenhaupt, K. Pei, S. Ye, V. Birss, Novel Mesoporous Carbon Supports for PEMFC Catalysts, Catalysts 5 (2015) 1046–1067. https://doi.org/10.3390/catal5031046.
[21] Z. Hood, X. Yang, Y. Li, A. Naskar, M. Chi, P. Paranthaman, Conversion of Waste Tire Rubber into High-Value-Added Carbon Supports for Electrocatalysis, J. Electrochem. Soc. 165 (2018) H881–H888. https://doi.org/10.1149/2.1081813jes.
[22] M. Boota, M.P. Paranthaman, A.K. Naskar, Y. Li, K. Akato, Y. Gogotsi, Waste Tire Derived Carbon–Polymer Composite Paper as Pseudocapacitive Electrode with Long Cycle Life, ChemSusChem 8 (2015) 3576–3581. https://doi.org/10.1002/cssc.201500866.
[23] M. Zhi, F. Yang, F. Meng, M. Li, A. Manivannan, N. Wu, Effects of Pore Structure on Performance of An Activated-Carbon Supercapacitor Electrode Recycled from Scrap

Waste Tires, ACS Sustain. Chem. Eng. 2 (2014) 1592–1598. https://doi.org/10.1021/sc500336h.
[24] A. Golawska, Tire Waste Statistics You Need To Know, Contec (2024). https://contec.tech/tire-waste-statistics-need-to-know/ (accessed April 11, 2024).
[25] J.R. Innes, One-and-a-half billion tyres wasted annually – there's a better way to recycle them, The Conversation (2024). http://theconversation.com/one-and-a-half-billion-tyres-wasted-annually-theres-a-better-way-to-recycle-them-208967 (accessed April 11, 2024).
[26] J. Gnanaraj, R. Lee, A. Levine, J. Wistrom, S. Wistrom, Y. Li, J. Li, K. Akato, A. Naskar, P. Paranthaman, Sustainable Waste Tire Derived Carbon Material as a Potential Anode for Lithium-Ion Batteries, Sustainability 10 (2018) 2840. https://doi.org/10.3390/su10082840.
[27] M. de Assumpção Pereira-da-Silva, F.A. Ferri, Scanning Electron Microscopy, in: A.L. Da Róz, M. Ferreira, F. de Lima Leite, O.N. Oliveira (Eds.), Nanocharacterization Techniques, William Andrew Publishing, 2017: pp. 1–35. https://doi.org/10.1016/B978-0-323-49778-7.00001-1.
[28] J. Campbell, S. Burkitt, N. Dong, C. Zavaleta, Nanoparticle characterization techniques, in: E.J. Chung, L. Leon, C. Rinaldi (Eds.), Nanoparticles for Biomedical Applications, Elsevier, 2020: pp. 129–144. https://doi.org/10.1016/B978-0-12-816662-8.00009-6.
[29] T. Schmid, Scanning-electron microscopy, Fakultäten an Der HU (2017). https://fakultaeten.hu-berlin.de/en/mnf/forschung_internationales/grs/salsa/p-a-labs/application-lab/instrumentation/a-labs-sem (accessed April 12, 2024).
[30] A.A. Bunaciu, E. UdriŞTioiu, H. Aboul-Enein, X-Ray Diffraction: Instrumentation and Applications, CRC Cr. Rev. Anal. Chem. 45 (2015) 289–299. https://doi.org/10.1080/10408347.2014.949616.
[31] N. Raval, R. Maheshwari, D. Kalyane, S.R. Youngren-Ortiz, M.B. Chougule, R.K. Tekade, Importance of Physicochemical Characterization of Nanoparticles in Pharmaceutical Product Development, in: R.K. Tekade (Ed.), Basic Fundamentals of Drug Delivery, Academic Press, 2019: pp. 369–400. https://doi.org/10.1016/B978-0-12-817909-3.00010-8.
[32] C. Suryanarayana, M.G. Norton, X-Ray Diffraction, Springer US, Boston, MA, 1998. https://doi.org/10.1007/978-1-4899-0148-4.
[33] Crystallography. Scattering and diffraction. The Bragg's Law, (2024). https://www.xtal.iqf.csic.es/Cristalografia/parte_05_5-en.html (accessed April 14, 2024).
[34] S. Fatimah, R. Ragadhita, D.F.A. Husaeni, A.B.D. Nandiyanto, How to Calculate Crystallite Size from X-Ray Diffraction (XRD) using Scherrer Method, ASEAN J. Sci. Eng. 2 (2021) 65–76. https://doi.org/10.17509/ajse.v2i1.37647.
[35] S. Ebnesajjad, Surface and Material Characterization Techniques, in: Surface Treatment of Materials for Adhesion Bonding, Elsevier, 2006: pp. 43–75. https://doi.org/10.1016/B978-081551523-4.50006-7.

[36] J. Mathias, Applications of Thermogravimetric Analysis, Innovatech Labs (2022). https://www.innovatechlabs.com/newsroom/2333/applications-thermogravimetric-analysis/ (accessed April 18, 2024).
[37] Y. Yang, H. Jia, Z. Cao, H. Zhang, P. Xu, X. Li, Integrated Resonant Cantilever with Dual Thermoanalytical Functions of Thermogravimetric Analysis and Differential Thermal Analysis, in: 2024 IEEE 37th International Conference on Micro Electro Mechanical Systems (MEMS), 2024: pp. 209–212. https://doi.org/10.1109/MEMS58180.2024.10439602.
[38] S.P. Rigby, Gas Sorption, Springer International Publishing, Cham, 2020: pp. 15-48. https://doi.org/10.1007/978-3-030-47418-8_2.
[39] B. Alinaghipour, C. Falamaki, Modified BET theory for actual surfaces: implementation of surface curvature, Phys. Chem. Chem. Phys. 25 (2023) 8424–8438. https://doi.org/10.1039/D2CP05575A.
[40] K.S.W. Sing, Reporting physisorption data for gas/solid systems with special reference to the determination of surface area and porosity (Recommendations 1984), Pure. Appl. Chem. 57 (1985) 603–619. https://doi.org/10.1351/pac198557040603.
[41] D. Dollimore, P. Spooner, A. Turner, The bet method of analysis of gas adsorption data and its relevance to the calculation of surface areas, Surf. Technol. 4 (1976) 121–160. https://doi.org/10.1016/0376-4583(76)90024-8.
[42] Y.S. Choudhary, L. Jothi, G. Nageswaran, Climent, in: T. Sabu, T. Raju, M. Raghvendra Kumar (Eds.), Spectroscopic Methods for Nanomaterials Characterization, Elsevier, 2017: pp. 19–54. https://doi.org/10.1016/B978-0-323-46140-5.00002-9.
[43] V. Climent, J.M. Feliu, Cyclic Voltammetry, in: K. Wandelt (Ed.), Encyclopedia of Interfacial Chemistry, Elsevier, 2018: pp. 48–74. https://doi.org/10.1016/B978-0-12-409547-2.10764-4.
[44] Y. Li, P.-L. Tremblay, T. Zhang, Anode Catalysts and Biocatalysts for Microbial Fuel Cells, in: Progress and Recent Trends in Microbial Fuel Cells, Elsevier, 2018: pp. 143–165. https://doi.org/10.1016/B978-0-444-64017-8.00009-9.
[45] A.J. Bard, L.R. Faulkner, Electrochemical Methods, 2nd ed., Wiley, New York, 2001: pp. 45-53.
[46] J. Wang, Analytical Electrochemistry, Wiley-VCH, Canada, 2000: pp. 28-40, https://www.academia.edu/14714519/ANALYTICAL_ELECTROCHEMISTRY_SECOND_EDITION (accessed May 23, 2022).
[47] K. Shinozaki, J.W. Zack, R.M. Richards, B.S. Pivovar, S.S. Kocha, Oxygen Reduction Reaction Measurements on Platinum Electrocatalysts Utilizing Rotating Disk Electrode Technique: I. Impact of Impurities, Measurement Protocols and Applied Corrections, J. Electrochem. Soc. 162 (2015) F1144. https://doi.org/10.1149/2.1071509jes.
[48] R. Sharma, S. Gyergyek, S.M. Andersen, Critical thinking on baseline corrections for electrochemical surface area (ECSA) determination of Pt/C through H-adsorption/H-desorption regions of a cyclic voltammogram, Applied Catalysis B: Environmental 311 (2022) 121351. https://doi.org/10.1016/j.apcatb.2022.121351.

[49] S. Trasatti, O.A. Petrii, Real surface area measurements in electrochemistry, J. Electroanal Chem. 327 (1992) 353–376. https://doi.org/10.1016/0022-0728(92)80162-W.
[50] C. Du, Q. Tan, G. Yin, J. Zhang, Rotating Disk Electrode Method, in: W. Xing, Y. Geping, J. Zhang (Eds.), Rotating Electrode Methods and Oxygen Reduction Electrocatalysts, Elsevier, 2014: pp. 171–198. https://doi.org/10.1016/B978-0-444-63278-4.00005-7.
[51] H.-L. Chou, B.-J. Hwang, C.-L. Sun, Catalysis in Fuel Cells and Hydrogen Production, in: S.L. Suib (Ed.), New and Future Developments in Catalysis, Elsevier, Amsterdam, 2013: pp. 217–270. https://doi.org/10.1016/B978-0-444-53880-2.00014-4.
[52] H. Liu, J. Zhang, Electrocatalysis of Direct Methanol Fuel Cells: From Fundamentals to Applications, 2009. https://doi.org/10.1002/9783527627707.
[53] N.M. Markovic, H.A. Gasteiger, P.N. Ross, Oxygen Reduction on Platinum Low-Index Single-Crystal Surfaces in Sulfuric Acid Solution: Rotating Ring-Pt(hkl) Disk Studies, J. Phys. Chem. 99 (1995) 3411–3415. https://doi.org/10.1021/j100011a001.
[54] K. Vaarmets, J. Nerut, E. Härk, E. Lust, Electrochemical and physical characterisation of Pt-nanocluster activated molybdenum carbide derived carbon electrodes, Electrochim. Acta 104 (2013) 216–227. https://doi.org/10.1016/j.electacta.2013.04.097.
[55] J. Nerut, P. Teppor, R. Palm, R. Jäger, T. Thomberg, K. Tuul, M. Koppel, J. Aruväli, A. Kikas, J. Mondal, V. Iakimov, E. Lust, Characterisation of Novel Nitrogen Doped Reduced Graphene Oxide, ECS Trans. 108 (2022) 99–109. https://doi.org/10.1149/10807.0099ecst.
[56] Shilpa, R. Kumar, A. Sharma IITK, Morphologically tailored activated carbon derived from waste tires as high-performance anode for Li-ion battery, J. Appl. Electrochem. 48 (2018) 1–13. https://doi.org/10.1007/s10800-017-1129-3.
[57] P. Teppor, R. Jäger, M. Koppel, O. Volobujeva, R. Palm, M. Månsson, E. Härk, Z. Kochovski, J. Aruväli, K. Kooser, S. Granroth, T. Käämbre, J. Nerut, E. Lust, Unlocking the porosity of Fe–N–C catalysts using hydroxyapatite as a hard template en route to eco-friendly high-performance AEMFCs: Journal of Power Sources, J. Power. Sources. 591 (2024). https://doi.org/10.1016/j.jpowsour.2023.233816.
[58] A. Raudsepp, R. Jäger, J. Nerut, P. Valk, P. Teppor, M. Koppel, J. Aruväli, J. Laanemäe, W. Lobjakas, E. Lust, Preparation of Membrane Electrode Assemblies Using Waste Tire Derived Carbon Supported Platinum Catalyst: ECS transactions, in: The Electrochemical Society, 2023: pp. 51–62.
[59] J. Laanemäe, R. Jäger, P. Teppor, O. Volobujeva, E. Lust, Waste Tire Derived Carbon Support for Non-Platinum-Group Metal Catalyst Materials for Oxygen Reduction Reaction in Alkaline Medium: ECS transactions, in: The Electrochemical Society, 2023: pp. 63–72.
[60] M. Muhyuddin, D. Testa, R. Lorenzi, G.M. Vanacore, F. Poli, F. Soavi, S. Specchia, W. Giurlani, M. Innocenti, L. Rosi, C. Santoro, Iron-based electrocatalysts derived from scrap tires for oxygen reduction reaction: Evolution of synthesis-structure-performance relationship in acidic, neutral and alkaline media, Electrochim. Acta 433 (2022) 141254. https://doi.org/10.1016/j.electacta.2022.141254.

[61] K. Vaarmets, J. Nerut, S. Sepp, R. Kanarbik, E. Lust, Accelerated Durability Tests of Molybdenum Carbide Derived Carbon Based Pt Catalysts for PEMFC, J. Electrochem. Soc. 164 (2017) F338–F346. https://doi.org/10.1149/2.1021704jes.
[62] Y. Shao, S. Zhang, R. Kou, X. Wang, C. Wang, S. Dai, V. Viswanathan, J. Liu, Y. Wang, Y. Lin, Noncovalently functionalized graphitic mesoporous carbon as a stable support of Pt nanoparticles for oxygen reduction, J. Power Sources 195 (2010) 1805–1811. https://doi.org/10.1016/j.jpowsour.2009.10.036.
[63] R. Kou, Y. Shao, D. Mei, Z. Nie, D. Wang, C. Wang, V.V. Viswanathan, S. Park, I.A. Aksay, Y. Lin, Y. Wang, J. Liu, Stabilization of Electrocatalytic Metal Nanoparticles at Metal−Metal Oxide−Graphene Triple Junction Points, J. Am. Chem. Soc. 133 (2011) 2541–2547. https://doi.org/10.1021/ja107719u.
[64] J. Quinson, M. Inaba, S. Neumann, A.A. Swane, J. Bucher, S.B. Simonsen, L. Theil Kuhn, J.J.K. Kirkensgaard, K.M.Ø. Jensen, M. Oezaslan, S. Kunz, M. Arenz, Investigating Particle Size Effects in Catalysis by Applying a Size-Controlled and Surfactant-Free Synthesis of Colloidal Nanoparticles in Alkaline Ethylene Glycol: Case Study of the Oxygen Reduction Reaction on Pt, ACS Catal. 8 (2018) 6627–6635. https://doi.org/10.1021/acscatal.8b00694.
[65] P. Valk, J. Nerut, R. Kanarbik, I. Tallo, J. Aruväli, E. Lust, Synthesis and Characterization of Platinum-Cerium Oxide Nanocatalysts for Methanol Oxidation, J. Electrochem. Soc. 165 (2018) F315–F323. https://doi.org/10.1149/2.0781805jes.
[66] M. Inaba, J. Quinson, J.R. Bucher, M. Arenz, On the Preparation and Testing of Fuel Cell Catalysts Using the Thin Film Rotating Disk Electrode Method, Jove-J. Vis Exp. (2018) e57105. https://doi.org/10.3791/57105.
[67] Y. Garsany, O.A. Baturina, K.E. Swider-Lyons, S.S. Kocha, Experimental Methods for Quantifying the Activity of Platinum Electrocatalysts for the Oxygen Reduction Reaction, Anal. Chem. 82 (2010) 6321–6328. https://doi.org/10.1021/ac100306c.
[68] M. Klingele, B. Britton, M. Breitwieser, S. Vierrath, R. Zengerle, S. Holdcroft, S. Thiele, A completely spray-coated membrane electrode assembly, Electrochem. Commun. 70 (2016) 65–68. https://doi.org/10.1016/j.elecom.2016.06.017.
[69] S.A. Mauger, J.R. Pfeilsticker, M. Wang, S. Medina, A.C. Yang-Neyerlin, K.C. Neyerlin, C. Stetson, S. Pylypenko, M. Ulsh, Fabrication of high-performance gas-diffusion-electrode based membrane-electrode assemblies, J. Power Sources 450 (2020) 227581. https://doi.org/10.1016/j.jpowsour.2019.227581.
[70] A. Hanna, K.S. Loh, W. Wong, R. Mohamad Yunus, T.K. Lee, A. Ahmad, S. Chong, Review of Chitosan-Based Polymers as Proton Exchange Membranes and Roles of Chitosan-Supported Ionic Liquids, Int. J. Mol. Sci. 21 (2020) 632. https://doi.org/10.3390/ijms21020632.
[71] S. Paul, M. Rahaman, S.K. Ghosh, A. Katheria, T.K. Das, S. Patel, N.C. Das, Recycling of waste tire by pyrolysis to recover carbon black: an alternative reinforcing filler, J Mater Cycles Waste Manag 25 (2023) 1470–1481. https://doi.org/10.1007/s10163-023-01635-6.

[72] S. Mostoni, Milana, B. Di Credico, D'Arienzo, Scotti, Zinc-Based Curing Activators: New Trends for Reducing Zinc Content in Rubber Vulcanization Process, Catalysts 9 (2019) 664. https://doi.org/10.3390/catal9080664.
[73] S. Sattayanurak, J.W.M. Noordermeer, K. Sahakaro, W. Kaewsakul, W.K. Dierkes, A. Blume, Silica-Reinforced Natural Rubber: Synergistic Effects by Addition of Small Amounts of Secondary Fillers to Silica-Reinforced Natural Rubber Tire Tread Compounds, Advances in Materials Science and Engineering 2019 (2019) e5891051. https://doi.org/10.1155/2019/5891051.
[74] K. Longkaew, A. Gibaud, W. Tessanan, P. Daniel, P. Phinyocheep, Spherical CaCO3: Synthesis, Characterization, Surface Modification and Efficacy as a Reinforcing Filler in Natural Rubber Composites, Polymers 15 (2023) 4287. https://doi.org/10.3390/polym15214287.
[75] X. Wang, L. Zhou, J. Li, N. Han, X. Li, G. Liu, D. Jia, Z. Ma, G. Song, X. Zhu, Z. Peng, L. Zhang, The Positive Effect of ZnS in Waste Tire Carbon as Anode for Lithium-Ion Batteries, Materials (Basel) 14 (2021) 2178. https://doi.org/10.3390/ma14092178.
[76] T. Ungár, J. Gubicza, G. Ribárik, C. Pantea, T.W. Zerda, Microstructure of carbon blacks determined by X-ray diffraction profile analysis, Carbon 40 (2002) 929–937. https://doi.org/10.1016/S0008-6223(01)00224-X.
[77] P. Valk, J. Nerut, R. Kanarbik, J. Aruväli, P. Paiste, I. Tallo, E. Lust, Synthesis and Characterization of Platinum-Praseodymium Oxide Nanocatalysts for Methanol Oxidation, ECS Trans. 86 (2018) 649–658. https://doi.org/10.1149/08613.0649ecst.
[78] B.G. Kelly, A.B. Loether, A.D. DiChiara, R.W. Henning, M.F. DeCamp, K.M. Unruh, Lattice parameter evolution in Pt nanoparticles during photo-thermally induced sintering and grain growth, J. Phys. Chem. Solids 108 (2017) 104–108. https://doi.org/10.1016/j.jpcs.2017.04.009.
[79] F. Cataldo, On the characterisation of carbon black from tire pyrolysis, Fullerenes, Nanotubes and Carbon Nanostructures 28 (2020) 368–376. https://doi.org/10.1080/1536383X.2019.1685983.
[80] M. Passaponti, L. Rosi, M. Savastano, W. Giurlani, H.A. Miller, A. Lavacchi, J. Filippi, G. Zangari, F. Vizza, M. Innocenti, Recycling of waste automobile tires: Transforming char in oxygen reduction reaction catalysts for alkaline fuel cells, J. Power Sources 427 (2019) 85–90. https://doi.org/10.1016/j.jpowsour.2019.04.067.
[81] M. Passaponti, L. Lari, M. Bonechi, F. Bruni, W. Giurlani, G. Sciortino, L. Rosi, L. Fabbri, M. Vizza, V.K. Lazarov, C. Fontanesi, M. Innocenti, Optimisation Study of Co Deposition on Chars from MAP of Waste Tyres as Green Electrodes in ORR for Alkaline Fuel Cells, J. Power Sources 13 (2020) 5646. https://doi.org/10.3390/en13215646.
[82] H.Q.V. Nguyen, J. Nerut, H. Kasuk, V. Grozovski, T. Thomberg, I. Tallo, R. Palm, M. Koppel, T. Romann, R. Härmas, J. Aruväli, M. Külaviir, E. Lust, Oxygen Reduction Reaction on Chromium Carbide-Derived Carbons, Russ. J. Electrochem. 58 (2022) 781–797. https://doi.org/10.1134/S1023193522090130.

[83] M. Ta, J. Nerut, T. Tooming, T. Thomberg, A. Jänes, E. Lust, Oxygen Electroreduction on Platinum Nanoparticles Deposited onto D-Glucose Derived Carbon, Journal of The Electrochemical Society 162 (2015) F651–F660. https://doi.org/10.1149/2.0231507jes.

[84] F. Si, Y. Zhang, L. Yan, J. Zhu, M. Xiao, C. Liu, W. Xing, J. Zhang, 4 - Electrochemical Oxygen Reduction Reaction, in: W. Xing, G. Yin, J. Zhang (Eds.), Rotating Electrode Methods and Oxygen Reduction Electrocatalysts, Elsevier, Amsterdam, 2014: pp. 133–170. https://doi.org/10.1016/B978-0-444-63278-4.00004-5.

[85] T. Shinagawa, A.T. Garcia-Esparza, K. Takanabe, Insight on Tafel slopes from a microkinetic analysis of aqueous electrocatalysis for energy conversion, Sci Rep 5 (2015) 13801. https://doi.org/10.1038/srep13801.

[86] M. Gara, K.R. Ward, R.G. Compton, Nanomaterial modified electrodes: evaluating oxygen reduction catalysts, Nanoscale 5 (2013) 7304. https://doi.org/10.1039/c3nr01940c.

[87] C. He, S. Desai, G. Brown, S. Bollepalli, PEM Fuel Cell Catalysts: Cost, Performance, and Durability, Electrochemical Society Interface 14 (2005). https://doi.org/10.1149/2.F07053IF.

[88] P.K. Mohanta, M.S. Ripa, F. Regnet, L. Jörissen, Impact of Membrane Types and Catalyst Layers Composition on Performance of Polymer Electrolyte Membrane Fuel Cells, ChemistryOpen 9 (2020) 607–615. https://doi.org/10.1002/open.202000089.

Acknowledgements

The author thanks her supervisors, PhD Rutha Jäger and PhD Jaak Nerut. The author would also like to thank Mr. Joel Indrek Martin Laanemäe for synthesising the waste tire derived carbon, Mr. Jaan Aruväli for performing XRD, PhD Olga Volobujeva for SEM and SEM-EDX analysis (TalTech, Institute of Materials and Environmental Technology), and PhD Patrick Teppor for his assistance with pyrolysis. Special thanks to MSc Wiljar Lobjakas, who was helpful at every stage of the completion of this thesis.

This work was supported

- by the Estonian Research Council (Proof-of-Concept Grant EAG273 and Personal Research Grant PRG676),
- by the project ”Increasing the knowledge intensity of Ida-Viru entrepreneurship” co-funded by the European Union (ÕÜF1), and
- by the Estonian Ministry of Education and Research (Center of Excellence TK210 and TK141).

Non-Exclusive Licence to Reproduce the Thesis and Make the Thesis Public

I, **Annabel Raudsepp**,

1. grant the University of Tartu a free permit (non-exclusive licence) to reproduce, for the purpose of preservation, including for adding to the DSpace digital archives until the expiry of the term of copyright, my thesis

Characterisation of Platinum Catalysts Based on Waste Tire Derived Carbons

supervised by **PhD Rutha Jäger and PhD Jaak Nerut**.

2. grant the University of Tartu a permit to make the thesis specified in point 1 available to the public via the web environment of the University of Tartu, including via the DSpace digital archives, under the Creative Commons licence CC BY NC ND 4.0, which allows, by giving appropriate credit to the author, to reproduce, distribute the work and communicate it to the public, and prohibits the creation of derivative works and any commercial use of the work until the expiry of the term of copyright.

3. I am aware of the fact that the author retains the rights specified in points 1 and 2.

4. I confirm that granting the non-exclusive licence does not infringe other persons' intellectual property rights or rights arising from the personal data protection legislation.

/signed digitally/

Annabel Raudsepp

May 30, 2024